Chapter 11
Laser Cladding of Ni-Based Superalloys

Gopinath Muvvala, Sagar Sarkar, and Ashish Kumar Nath

11.1 Introduction to Ni-Based Alloys

Among all the available engineering materials, nickel and its alloys have gained wide popularity due to their ability to withstand severe operating conditions like corrosive environments both in aqueous and at high temperature, high strength at ambient and elevated temperatures, and combination of these. Apart from this, its ability to be diluted by a large number of elements or materials and retaining its ductility and strength from cryogenic to solidus temperature with the matrix being austenitic throughout the temperature range has made it a potential candidate for a wide range of applications. With appropriate alloying elements and elevated physical properties, Ni-based alloys find wide applications in marine, nuclear, power plant, petrochemical, and aerospace industries. A typical application of Ni-based alloys in gas turbine is illustrated in Fig. 11.1 (Leary et al. 2018). Air from the inlet enters the compressor unit where its pressure is increased to almost 24 times in 15 stages, each one consisting of a set of rotor and stator (Cemal et al. 2012; Eliaz et al. 2002). From the compressor, air enters at a high pressure into the combustion chamber where fuel is injected and burned raising the temperature to as high as 1930 °C, which is cooled close to 1100 °C, limited by the maximum operating temperature of materials, essentially a nickel-based alloy (Leary et al. 2018; Cemal et al. 2012). This gives a glimpse of severity of atmosphere in which nickel-based alloys can operate.

G. Muvvala (✉)
Department of Mechanical and Aerospace Engineering, Indian Institute of Technology Hyderabad, Sangareddy, India
e-mail: mgopinath@iith.ac.in

S. Sarkar · A. K. Nath
Department of Mechanical Engineering, Indian Institute of Technology Kharagpur, Kharagpur, India
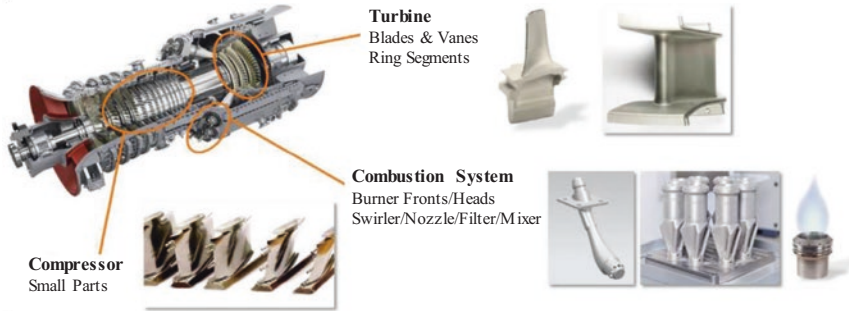e-mail: aknath@mech.iitkgp.ac.in

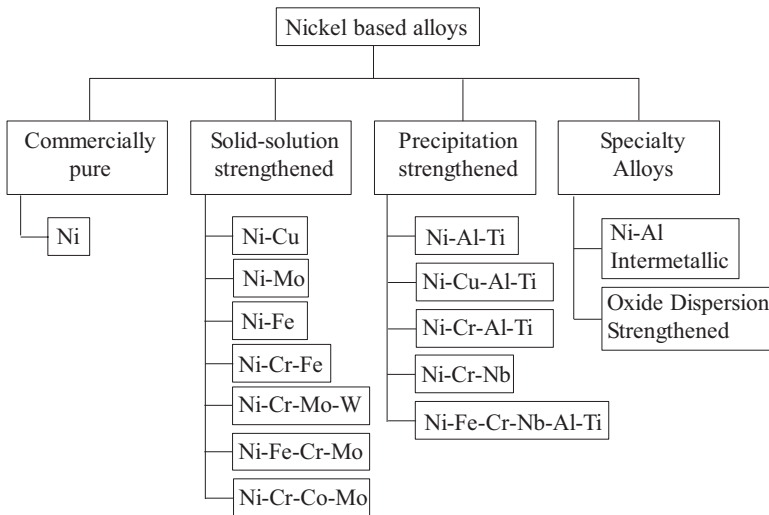**Fig. 11.1** Inconel superalloys in gas turbine applications (Leary et al. 2018)

Fig. 11.2 Classification of nickel-based superalloys (DuPont et al. 2009)

11.1.1 Classification of Ni-Based Superalloys

Nickel-based superalloys can be broadly classified into four categories, as shown in Fig. 11.2. Commercially pure Ni alloys contain nickel (> 99%) and are mostly used for their corrosion resistance in caustic environments. However, they suffer from low strength and hardness. Solid solution-strengthened alloys are used in applications where a combination of moderate strength and excellent corrosion resistance is required. These are primarily strengthened by the addition of substitutional alloying elements such as Cu, Mo, Fe, Cr, and W, as shown in Fig. 11.2, which provide solid solution strengthening of austenitic microstructure. Precipitation-strengthened Ni-based alloys are used in applications where the combination of both high strength and excellent corrosion resistance is important. The development of these alloys

made the "jet age" possible. Compared to solid solution-strengthened alloys, the physical metallurgy of precipitation-strengthened Ni-based alloys is quite complex. These alloys along with solid solution strengthening elements contain Ti, Al, and Nb for precipitate formation; Cr, Al, and Ta for oxidation resistance; Cr, La, and Th for hot corrosion resistance; B and Zr for creep and stress rupture properties; and Hf for intermediate temperature ductility. A thorough study on the nickel-based alloys and their metallurgy is reported by DuPont et al. (2009) providing an exhaustive list of Ni alloys. Considering the context of this chapter and its relevance to laser cladding, the discussion is limited to two most commonly used solid solution- and precipitation-strengthened nickel-based alloys Inconel 625 and Inconel 718 and their metal matrix composite coatings.

11.2   Introduction to Laser Cladding

Before going to the details of laser cladding of nickel-based superalloys and the challenges involved, the different techniques of laser cladding and their fundamental differences are briefly discussed to understand the behaviors of same material under different processing conditions.

Laser cladding is a weld deposition technique in which the laser is used as a heat source to melt and deposit or overlay the feedstock, which may be in the form of wire or powder, onto a substrate. At the initial stage, it was very widely employed for depositing protective coatings against wear or corrosion. The main advantage stems from the fact that the process involves rapid heating followed by rapid cooling (10^3–10^6 °C/s) through self-quenching with minimum heat-affected zone and distortion and excellent metallurgical bonding. With time the process evolved into a multi-overlapped layer deposition technique which is now popularly known as **a**dditive **m**anufacturing (AM). In this process, the 3D computer-aided design (CAD) of a part to be built is first sliced into thin layers, usually 25–200 microns thick, and a 2D image of each layer is created in industry standard .stl format. Utilizing the data file, the part is built by depositing the desired material usually in the form of either powder or wire layer over layer. Utilizing laser as heat source and powder as feedstock, the process can be broadly classified into two methods, i.e., powder bed and blown powder methods, widely known as selective laser melting (SLM) and laser-engineered near net shaping (LENS) or direct metal laser deposition process (DMLD), respectively. As shown in Fig. 11.3a in powder bed method, a predefined thickness of power layer is spread on the surface of a build platform using a ceramic coater blade, followed by irradiation and melting by a focused laser beam in the selected areas as per the 2D layer data file. Again a layer of fresh powder is spread onto the already processed layer, and selective melting is carried out. The process is repeated until the component of desired height and shape is achieved. In DMLD process (Fig. 11.3b), the powder is fed coaxially along with the laser beam using a nozzle in such a way that the powder is heated up and fed into the molten pool created by the laser beam, which consolidates and forms an overlay. SLM process is

Fig. 11.3 Schematic of (**a**) SLM and (**b**) DMLD
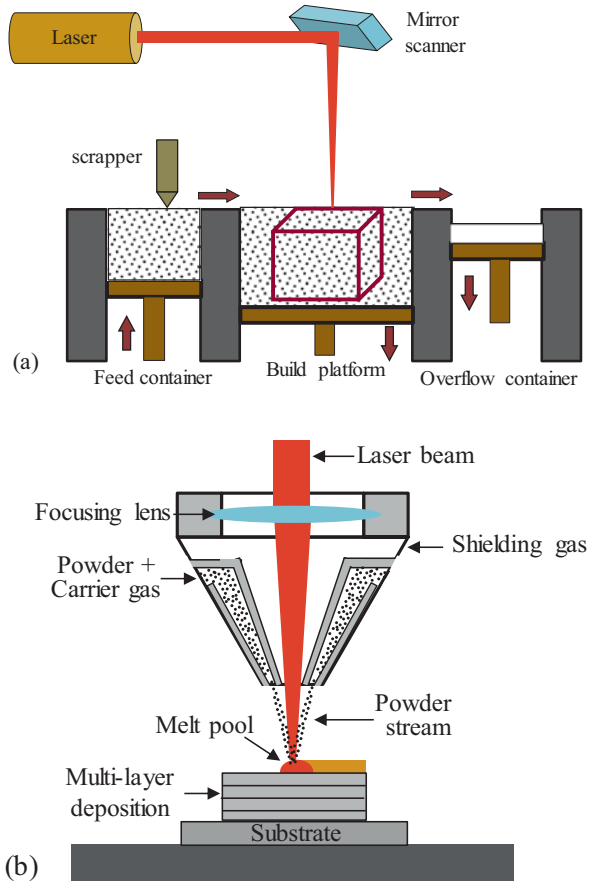
widely used to fabricate components with complex geometries and intricate shapes directly from the CAD model, whereas DMLD process is used for refurbishment of worn-out components and to deposit protective coatings. DMLD process has been further extended to fabricate the components directly also, similar to SLM. However, DMLD is second to SLM in terms of design complexity and dimension accuracy.

Apart from the differences in the method of deposition, it is very essential to understand typical variations in the process parameters which influence the thermal history of the molten pool, surface morphology, microstructure, and mechanical properties. Table 11.1 shows the process parameters and their typical values used in SLM and DMLD process. SLM process essentially involves smaller spot diameters and layer thickness of similar ranges. In DMLD process, the spot diameter is generally in the range of less than a mm to a few mm with resulting clad track dimension of similar range. This difference essentially dictates the cooling rates which significantly affect both microstructure and mechanical properties. Molten pool in SLM process experiences a typical cooling rate of 10^6 °C/s, while it is of the order of 10^3 °C/s in case of DMLD. Table 11.2 shows the achievable mechanical properties

Table 11.1 Process parameters in SLM and DMLD process (Wu et al. 2020; Qiu et al. 2019; Kang et al. 2018; Caiazzo 2018; Ramakrishnan and Dinda 2019)

Parameter	SLM	DMLD
Laser power (P) W	200–400	400–2000
Scan speed (V) mm/min	6×10^4–30×10^4	400–800
Spot diameter (d) mm	0.04–0.1	1–3
Power density ($4P/\pi d^2$) W/mm^2	2.5×10^4–32×10^4	~50–2500

Table 11.2 [a]Achievable mechanical properties in SLM and DMLD

Alloy	Process		Yield strength (MPa)	Ultimate tensile strength (MPa)	% Elongation	Hardness
Inconel 718	SLM (Chlebus et al. 2015)	XY	1159 ± 32	1137 ± 66	8 ± 6	463 ± 8
		Z	1074 ± 42	1320 ± 6	19 ± 2	
	SLM + HT (Wang et al. 2012)	XY	1131 ± 30	1319 ± 40	16 ± 6	470 ± 15
	SLM + HIP (Moussaoui et al. 2018)	XY	1150 ± 25	1350 ± 25	25 ± 2	475 ± 15
	DMLD (Zhang et al. 2015)	XY	720 ± 25	950 ± 25	17 ± 3	285 ± 15
	DMLD+HT	XY	1062	1270	6.5	255 ± 15
	Conventional (Rao et al. 2004)	Wrought	1098 ± 70	1335 ± 60	16 ± 5	400 ± 15
		Cast	758 ± 25	862 ± 25	5 ± 2	255 ± 50
Inconel 625	SLM (Marchese et al. 2020)	XY	780 ± 25	1050 ± 30	35 ± 3	354 ± 24
		Z	620 ± 25	880 ± 10	43 ± 3	
	SLM + HT (Marchese et al. 2020)	XY	780 ± 5	1060 ± 10	38 ± 6	342 ± 10
		Z	620 ± 10	980 ± 20	45 ± 6	
	DMLD (Paul et al. 2007)	XY	572 ± 25	920 ± 15	48 ± 2	255 ± 8 (Dinda et al. 2009)
		Z	568 ± 20	925 ± 12	46 ± 2	
	Conventional (Inconel 625 data sheet)	Annealed	534 ± 120	930 ± 100	45 ± 15	188 ± 24

[a]Under optimized parameters; HT, heat treated; HIP, hot isostatic pressing

of components fabricated by SLM and DMLD processes in comparison to conventional processes. It can be observed that under optimized conditions, the mechanical properties of parts built by AM process are close or even superior for some materials, like Ni alloys, than that obtained in conventional process. However, it is observed that the strength of DMLD-built parts is usually less than that of SLM-built parts. This is essentially due the different cooling rates in two processes which dictate the segregations in nickel-based superalloys.

11.3 Cooling Rate and Its Significance in Laser Cladding Process

11.3.1 Influence of Cooling Rate on Segregations in Ni-Based Superalloys

As discussed, nickel-based alloys are used in severe environments, like high-corrosive and high-temperature applications. This is made feasible by adding appropriate alloying elements as discussed in Sect. 11.1.1. It is therefore essential to ensure their proper distribution within the material, which otherwise results in degradation of its properties. The distribution of the alloying elements within the matrix highly depends on the thermal history they undergo during deposition processes. In order to elaborate and bring out a clear understanding of this, Inconel 718 is considered for the subsequent discussion. In Sect. 11.1.1, the alloying elements and their effects on the phase strengthening as well as mechanical properties were briefly discussed. However, it is important to understand their solubility in the metal matrix which is Ni-Cr-Fe, γ-matrix in case of Inconel 718.

Inconel 718 is basically a precipitation-strengthened nickel-based superalloy that contains Nb, Ti, and Al as alloying elements. During solidification process, it is expected to form γ' and γ'' phases, intermetallic phases based on Ni_3(Al,Ti), and Ni_3Nb having an ordered FCC L12 and a body-centered tetragonal DO_{22} structure, respectively, which are coherent with the γ-Ni solid solution matrix, i.e., Ni-Cr-Fe. The main principal strengthening mechanism involved is the antiphase boundary hardening arising from the coherent and ordered γ' and γ'' phases (Sims et al. 1987; Oblak et al. 1974). However, during the solidification process, the precipitation strengthening elements are susceptible to segregation owing to their low equilibrium distribution coefficients k as shown in Table 11.3 (Odabasi et al. 2010), which is defined as $k = C_S/C_L$, where C_S and C_L are the compositions of solid and liquid at the solid-liquid interface. However, the severity of this elemental segregation depends on the cooling or freezing rate, i.e., at higher cooling rates, the elements get trapped inside the γ-matrix improving the mechanical properties.

Figures 11.4 (Kou 2002) and 11.5 (Xiao et al. 2017) show the schematic of evolution of microstructure and its dependency on the cooling rate. During laser cladding process, the metal powder is melted along with a thin layer of substrate, both of which start solidifying as the laser beam proceeds ahead. Solidification initiates

Table 11.3 Average distribution coefficients

		k values of major elements						
Process		Nb	Al	Ti	Mo	Fe	Cr	Ni
Laser welding	2.9 kW, 39.94 mm/s	0.52	0.82	0.67	0.82	1.06	1.15	1.00
	1.5 kW, 11.85 mm/s	0.51	1.08	0.65	0.69	1.09	1.16	1.02
GTA		0.42	–	0.65	0.85	1.06	1.10	1.01
EB		0.53	–	0.71	0.69	1.05	1.04	0.96

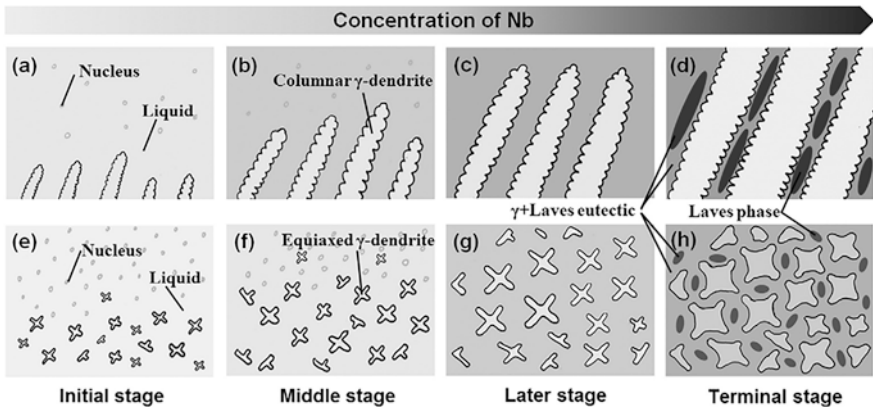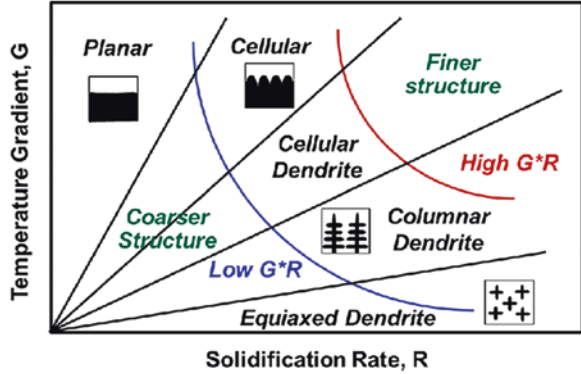**Fig. 11.4** Effect of G and R on the solidification morphology (Kou 2002)

Fig. 11.5 Schematic diagram of the microstructure evolution in Inconel 718 (Xiao et al. 2017)

from the interface of molten pool and the substrate due the heterogeneous nucleation. At the initial stage, the temperature gradients (G) and the solidification rate (R) will be quite large resulting in a planar, followed by columnar or epitaxial growth, as shown in Fig. 11.4. In other words, the cooling rate which is essentially the G × R product will be very high at the initial stage of solidification resulting in fine microstructure. As the solidification proceeds, the temperature gradient and the molten pool temperature decrease which results in the formation of homogeneous nucleation sites increasing the solidification rate and equiaxed grains. As shown in Fig. 11.5, in Inconel 718, the solidification process initiates as columnar γ austenitic phase (Ni-Cr-Fe), pushing the alloying elements (Nb) into the liquid phases because of their low distribution coefficient, as shown in Table. 11.3. As the process proceeds, the concentration of alloying elements in the liquid phase increases to such an extent where it starts solidifying, forming Laves phases. This mechanism of microstructural evolution is well reported by Muvvala et al. (2017c). Figure 11.6 shows the evolution of microstructure within the molten pool as discussed above. Three distinct zones can be identified clearly, where zone 1 shows the pure

Fig. 11.6 Transition from
epitaxial growth to
equiaxed grains in clad
zone near surface
(Muvvala et al. 2017c)
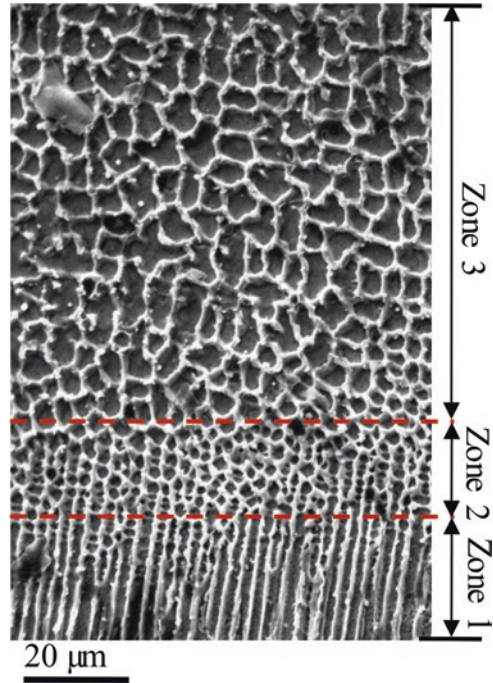
epitaxial/columnar growth, followed by transition zone 2 where the epitaxial growth terminates and equiaxed grains initiate and zone 3 consisting of fully defined equiaxed grains. However, depending on the cooling rate or the molten pool life-time, the segregation mechanism of the alloying elements varies in the laser cladding process. In case of columnar dendritic regions, where the cooling rate is expected to be maximum, alloying elements get entrapped in interdendritic regions, as shown in Fig. 11.5d, and at the top surface having relatively low cooling rates, equiaxed grains/γ-matrix start growing to sizes depending on the cooling rate pushing the alloying elements toward the grain boundaries, as shown in Fig. 11.5h. Therefore, the amount of segregation within a material essentially depends on the solidification rate which is controlled by the cooling rate and the temperature gradient. The faster the cooling rate, the lesser will be the segregation as rapid solidification results in entrapping these alloying elements. Thus, the cooling rate plays a critical role in dictating the evolution of microstructure and mechanical properties in laser cladding process.

Coming back to SLM and DMLD process, Fig. 11.7 shows the process map of cooling rate corresponding to each of these. As discussed before, it can be observed that the cooling rates are much higher in case of SLM compared to DMLD (denoted as LSF, laser solid forming) process, which essentially is the reason for superior mechanical properties in SLM parts, as shown in Table 11.2.
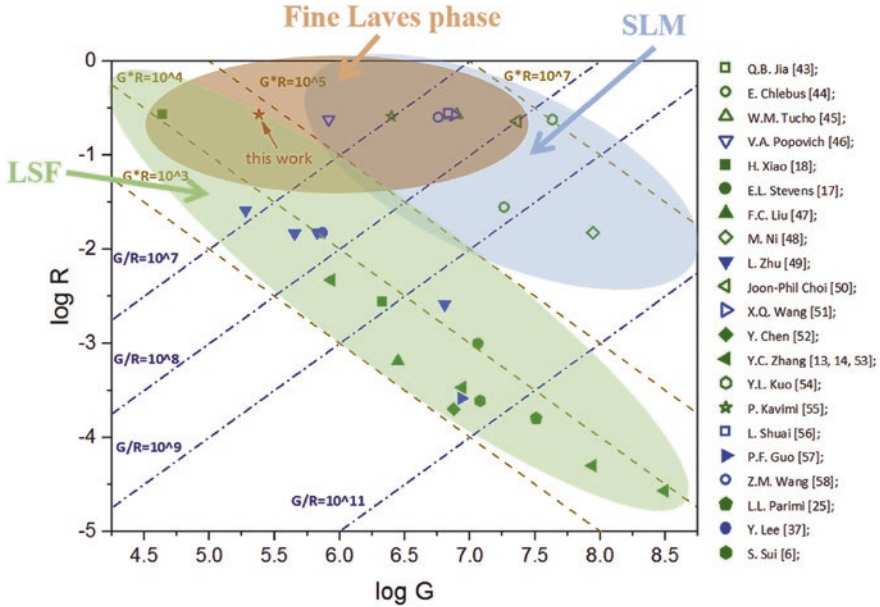
Fig. 11.7 The selection map of Laves phase morphology in Inconel 718 (Sui et al. 2019)

11.3.2 Effect of Elemental Segregation on Mechanical Properties

As discussed previously, Laves is a hexagonal close packed phase and is generally accepted as a form of $(Ni, Fe, Cr)_2(Nb, Mo, Ti)$. These are generally brittle in nature and deteriorate the mechanical properties or make the coating brittle (Gopinath et al. 2017). However, this essentially depends on their (Laves) size and distribution. Though the heat treatment could help in dissolving the Laves phase, followed by precipitation hardening, it has limitations in case of laser cladding. As laser cladding is widely used in the deposition of protective coatings or refurbishment of worn-out components, heat treatment may have adverse effects on the substrate microstructure and mechanical properties. Therefore, it is essential to control the size and shape of the Laves phase during the deposition itself. Sui et al. (2017a, b, 2019) and Ming et al. (2015) carried out a detailed research on Laves phase morphology and size on the deformation mechanism and their influence of mechanical properties at room and elevated temperatures. Laves phase deformation process includes two mechanisms, viz., fragmentation and separation from the γ-matrix as shown in Fig. 11.8. Fragmentation is essentially dominant in long-striped Laves phases during loading under room temperature due to stress concentration (Fig. 11.8a), whereas granular Laves being smaller in size move easily with γ-matrix increasing the ductility and reducing the chances of failure. Further, it can be observed that fragmentation is predominant even in case of fatigue crack
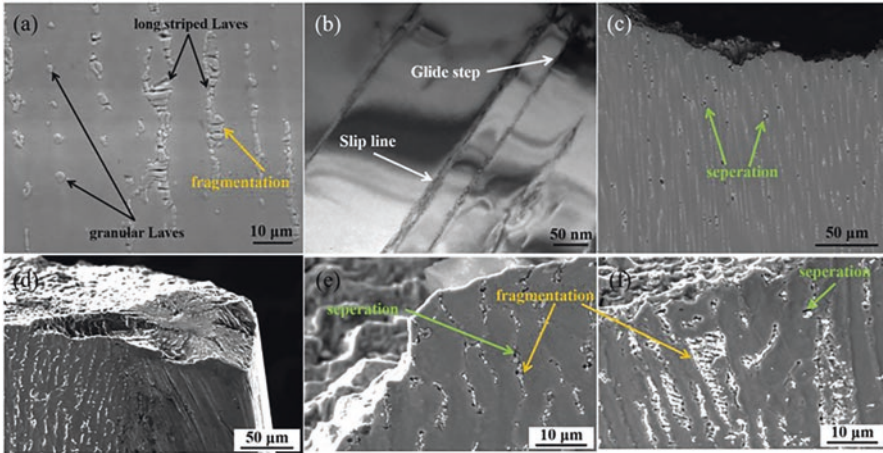
Fig. 11.8 Deformation behavior of Laves phase: (**a**) and (**b**) after the room temperature tensile test (Sui et al. 2017a); (**c**) after the stress rupture test ($T = 650\ °C$, $\sigma_a = 725$ MPa) (Ming et al. 2015); (**d**), (**e**), and (**f**) after high-cycle fatigue test ($T = 650\ °C$, $f = 110$ Hz, $R = 0.1$, $K_t = 1$, $\sigma_a = 750$ MPa) (Sui et al. 2017a); (**d**) in the fatigue source region; (**e**) in the fatigue crack propagation region; (**f**) in the fatigue final rupture region

propagation region (Fig. 11.8e) and the final fatigue rupture region (Fig. 11.8f). However, as shown in Fig. 11.8c, the separation is found to be the main dominating mechanism of failure in case of high-temperature rupture stress. This is also visible in case of Fig. 11.8e, f. This can be essentially attributed to the phase boundary weakening at high temperatures. Further, it is very essential to understand the influence of loading direction and orientation and shape of grains or segregating alloying elements. When the applied load or stress is parallel to the interface or boundary of the matrix and the Laves phase, high stress is required for separation, and therefore fragmentation could be dominant. However, when the applied stress is in perpendicular direction of the interface, separation could be dominant. Thus, in as-deposited additive manufactured components, directionality in mechanical properties always exists arising from the inhomogeneity in microstructure.

11.3.3 Parameters Affecting the Cooling Rate in Laser Cladding

From Sects. 11.3.1 and 11.3.2, it is evident that in laser cladding process the cooling rate or molten pool lifetime plays a significant role in determining the mechanical properties. Therefore, it is important to understand the process parameters that influence the cooling rate. Laser cladding involves a large number of process parameters, among them laser power, scan speed, spot diameter, and layer thickness or powder mass flow rate are the ones having the most significant influences, and
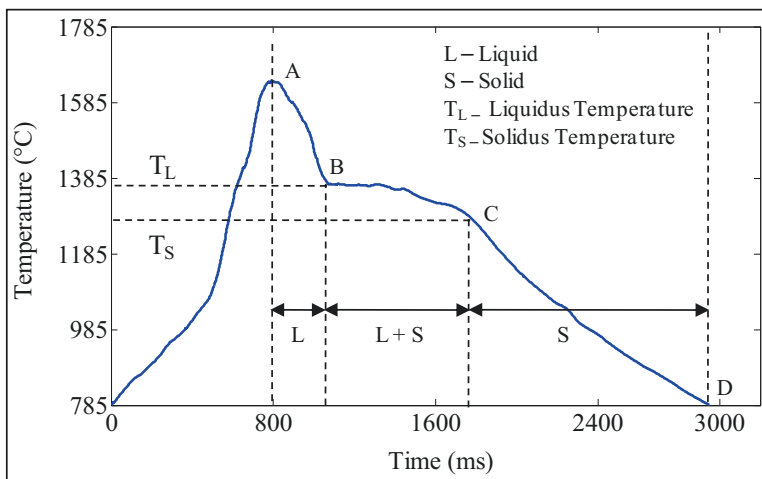
AB: Cooling of liquid phase   BC: Solidification shelf   CD: Cooling of solid phase

Fig. 11.9 Typical molten pool thermal cycle during the laser cladding process (Muvvala et al. 2017c)

therefore their effects are discussed in brief (Muvvala et al. 2017c). Muvvala et al. (2017c) carried out an experimental study on the influence of various process parameters on the molten pool thermal history which includes heating and cooling rates and molten pool lifetime using an IR pyrometer. Figure 11.9 shows a typical molten pool thermal history of a point during laser scan over a preplaced powder surface for cladding. It essentially consists of a heating cycle 0A and a cooling cycle AD. As the laser beam is scanned over the preplaced powder surface, the temperature at the point of laser irradiation rises rapidly melting the powder, and as the laser crosses over the point, it starts cooling. It can be observed that the cooling cycle exhibits several stages further which include cooling of molten pool (AB) and solidification shelf (BC) during which solidification process initiates (Point B) and ends (Point C) followed by solid state cooling (CD). Figure 11.10 shows typical relationships between heating and cooling rates and the molten pool lifetime (Nair et al. 2019). With increasing heating rate, cooling rate increases, and therefore the molten pool lifetime decreases which is beneficial for the mechanical properties of Ni-based coatings or components.

Figure 11.11 shows the effect of laser power and scan speed on the cooling rates (Muvvala et al. 2017c). It may be mentioned that good quality of cladding in terms of geometrical aspect and dilution was realized within the experimental range of process parameters. It can be observed that laser power has very little influence on cooling rate compared to the scan speed. At a given laser power, with the decrease of scan speed, the interaction time (ratio of laser beam diameter to scan speed) and the line energy (ratio of laser power to scan speed) both increase, and this tends to reduce the temperature gradient by heat conduction and therefore the cooling rate. However, at a given scan speed with increase in laser power, the energy density only
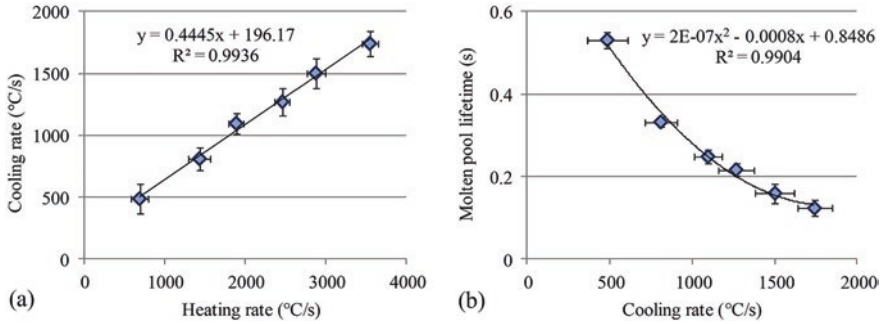
Fig. 11.10 Correlation between (**a**) heating and cooling rate and (**b**) cooling rate and molten pool lifetime (Nair et al. 2019)
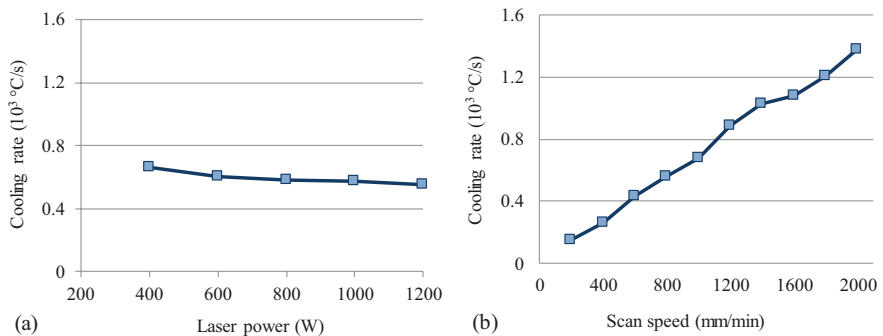

Fig. 11.11 Effect of (**a**) laser power and (**b**) scan speed on cooling rate (Muvvala et al. 2017c)

increases which tends to increase the melt pool temperature, but the onset of evaporation does not allow a significant increase in the peak temperature. Therefore, laser power has very little influence on the cooling rate. Further, the molten pool lifetime or cooling rate depends on the preplaced powder layer thickness also. As shown in Fig. 11.12, with an increase in layer thickness, the molten pool size or volume increases which tend to reduce the cooling rate. Figure 11.13 shows the variation in equiaxed grain size with the molten pool lifetime and cooling rate corresponding to different scan speeds, from which it is evident that faster cooling rates result in entrapment of alloying elements, while slower cooling rates result in severe segregations affecting the mechanical properties as discussed in previous sections.

11.3.4   *Effect of Process Parameters and Cooling Rates on Surface Properties*

Apart from the fabrication and refurbishment of components, laser cladding process is widely used in the field of surface engineering for depositing wear-resistant hardfacing and protective coatings against corrosion. Similar to the other mechanical

Fig. 11.12 Effect of layer
thickness on cooling rate
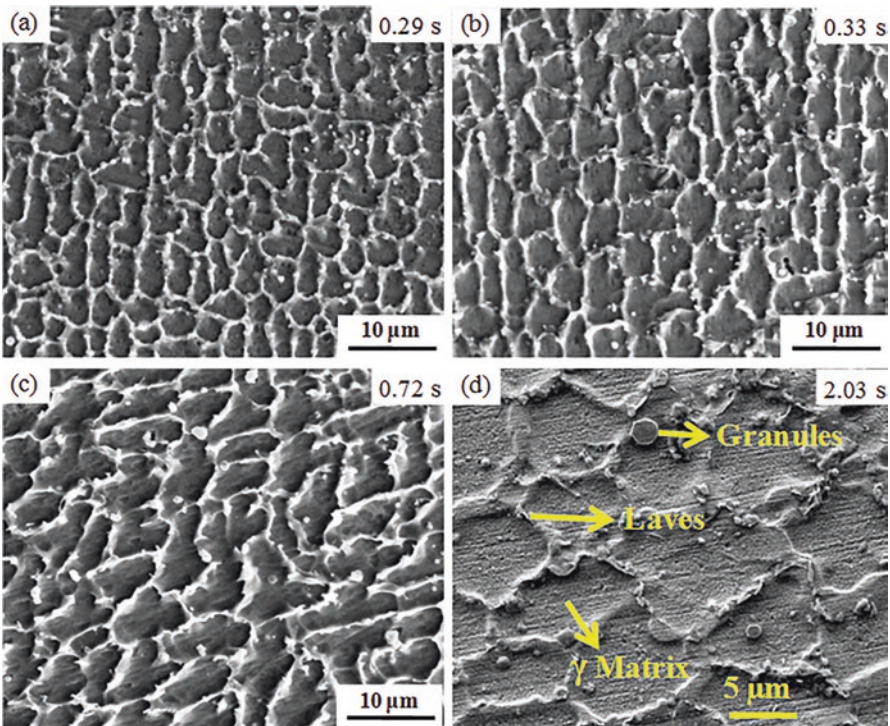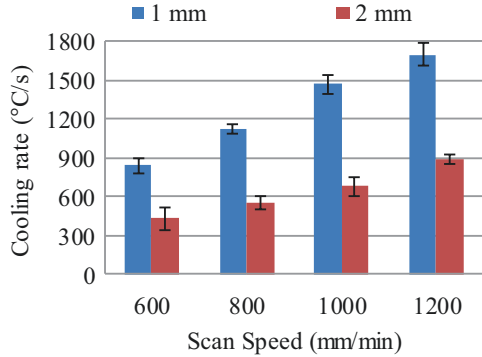(Muvvala et al. 2017c)

Fig. 11.13 Variation in equiaxed grain size with cooling rate, (**a**) 1050 °C/s, (**b**) 680 °C/s, (**c**) 435 °C/s, and (**d**) 152 °C/s corresponding to scan speeds of 1400, 1000, 600, and 200 mm/min, respectively

properties, cooling rate does play a significant role in determining the surface properties of coatings. Wolff et al. (2019) found that apart from the cooling rate, dilution is one of the major factors influencing the hardness in laser-deposited Inconel 718 on carbon steel. While the cooling rate was observed to reduce with the increase of laser power and powder flow rate due to the increase in the molten pool volume
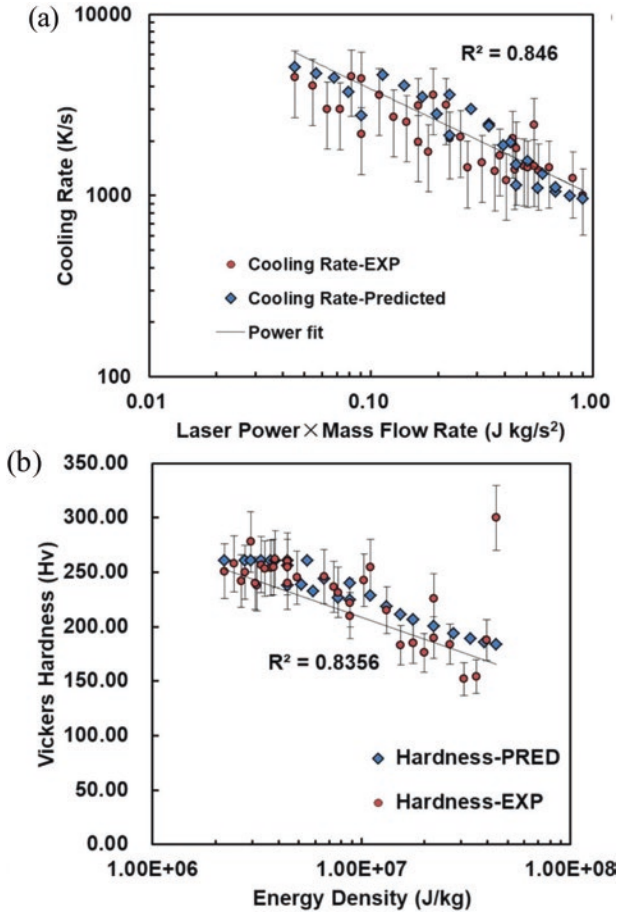
Fig. 11.14 (**a**) Effect of laser power and powder mass flow rate on cooling rate and (**b**) effect of energy density on hardness (Wolff et al. 2019)

(Fig.11.14a), the microhardness decreased with increasing laser energy per unit mass of powder deposited (Fig. 11.14b) which could be resulting from the decreased cooling rate, grain coarsening and elemental segregation, and increased dilution (Wolff et al. 2019).

In addition to the hardness, the corrosive properties of the coating also deteriorate for slower cooling rates. Luo et al. (2019) carried out a detailed research on corrosive behavior of selective laser-melted Inconel 718 with and without heat treatment and found that the Laves phase is detrimental to the corrosion properties of the coating. Figure 11.15 depicts schematically the corrosion mechanism in nickel-based alloys which experience segregation during the laser cladding process. As described earlier, Inconel 718 consists of γ-matrix as primary phase and γ′ and γ″ as secondary phases which tend to segregate at the grain boundary or interdendritic
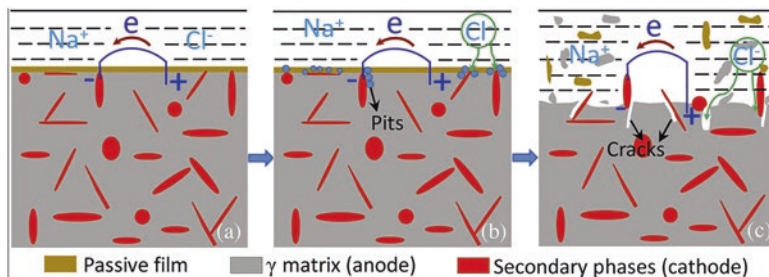
Fig. 11.15 Schematic presentations of galvanic coupling effect-induced corrosion micro-battery: (**a**) surface passivation, (**b**) formation of corrosion pits on surface passive film, (**c**) breakdown of surface passive film, dissolution of anode γ-matrix, and formation of cracks (Luo et al. 2019)

region during the deposition process. When a sample with such microstructure and phase distribution is exposed to the electric potential in a NaCl solution, the secondary phase serves as a cathode, while the γ-matrix serves as an anode (Luo et al. 2019) triggering the formation of abundant corrosion micro-batteries between Laves phases and γ-matrix due to the galvanic coupling effect, as depicted in Fig. 11.15. This results in preferential corrosion of γ-matrix. In addition, the substantial precipitation of carbides in the interdendritic region also facilitates the galvanic coupling effect. Further, this preferential corrosion also leads to the corrosion cracking, as shown in Fig. 11.15c, which is further favored by the in-built stresses.

Figure 11.16 shows the surface morphologies of Inconel 718 samples obtained by different processes after electrochemistry corrosion in 3.5 wt% NaCl solution. From Fig. 11.16a,b, the stress corrosion cracking is clearly evident in the case of as-built SLM samples. Further, in comparison to others, i.e., solution annealed and rolled samples (Fig. 11.16c–l), the corrosion cracks are markedly broadened. However, it can be observed that with heat treatment (Fig. 11.16c–h) the tendency of the corrosion cracking has completely reduced and limited to the interface of δ and γ phase which is essentially due to diffusion and dissolution of alloying element during the heat treatment process. However, as discussed previously, heat treatment may not be possible in all cases, especially in coating applications, and thus it is very essential to control the elemental segregations through proper selection of process parameters that could process the coating at rapid cooling rates.

11.4   Auxiliary Methods to Control Microstructure

From the above discussions, it is evident that controlling the microstructure and elemental segregations in nickel-based superalloys plays a vital role in dictating the mechanical properties of the laser-cladded protective coatings or components, though laser, being a rapid solidification process, still experiences elemental segregation. Also, rapid solidification results in directional solidification with

Fig. 11.16 Surface morphologies of Inconel 718 samples obtained by different processes after electrochemistry corrosion in 3.5 wt% NaCl solution: (**a**–**b**) SLM; heat treated for 1 h at (**c**–**d**) 940 °C; (**e**–**f**) 980 °C; (**g**–**h**) 1020 °C; (**i**–**j**) solution annealed at 980 °C × 1 h (air cooled) +720 °C × 8 h (furnace cooled, 50 °C/h) + 620 °C × 8 h (air cooled); (**k**–**l**) rolled (Luo et al. 2019)
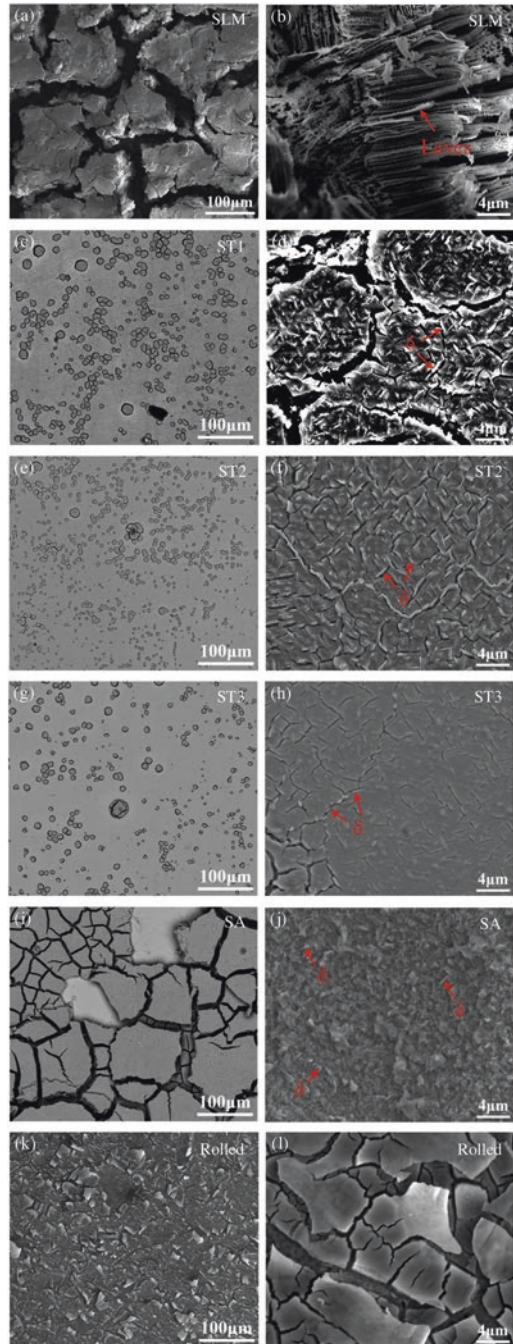
inhomogeneous microstructure creating anisotropy in the mechanical as well as corrosion properties with increased residual stresses leading to cracks. So far, effects of changing the laser process parameters and thus resultant cooling rate on microstructure have been discussed. However, these changes can only influence the external heat transfer boundary of the molten pool but not the direction of the fluid movement in the molten pool. Thermo-capillary convection is one of the critical factors which govern the mechanism of metal solidification. In order to control the convection movement of the molten pool, two major external fields, namely, ultrasonic vibration and electromagnetic fields, have been applied during laser material interaction. Also, the addition of rare earth elements which acts as a surfactant is also popular in laser cladding to modify the microstructure. In the subsequent sections, these methods are described in detail:

11.4.1 Electromagnetic Field-Assisted Laser Cladding

Electromagnetic force produced by electromagnetic field changes the heat conduction and convection of the molten pool. This method is superior to ultrasonic vibration in which attenuation of the ultrasonic field in the melt pool is an issue. Three different types of electromagnetic fields, namely, single electric field, single magnetic field, and electromagnetic compound field, have been used. Single magnetic field can be further subdivided into two categories: steady magnetic field and alternating magnetic field. Schematic of laser cladding under electromagnetic field is presented in Fig. 11.17. In case of single electric field, pulsed current is used, and its electromagnetic force compresses the molten pool, resulting in reduction in porosity in the clad layer. On the other hand, single magnetic field produces Lorentz force which causes resistance for the convection in the molten pool. This can change flow velocities inside the molten pool and inhibit the surface ripple (Wang et al. 2017b) and diffusion of elements in the molten pool (Chen et al. 2016). The stirring effect caused by the electromagnetic field makes the solute and temperature field homogenize in the molten pool and causes grain refinement. Further, increased fluidity of the liquid metal reduces viscosity of the molten pool and the possibility of shrinkage of the coating (Liu et al. 2013). Steady magnetic field cannot cause great influence on the flow of the molten pool, and therefore research on combined electromagnetic fields has been exploited. By combining electric field with magnetic field, the Lorentz force can be effectively controlled to change the direction, intensity, and frequency of the magnetic and electric fields (Wang et al. 2015a). This can reduce the porosity of the clad layers (Zhang et al. 2018) and change the positions of the strengthening phase particles in the melt pool (Wang et al. 2017). A schematic showing force analysis diagram of a point in molten pool with and without electromagnetic field is presented in Fig. 11.18.

Ni-based coating such as Ni-Cr-B-Si alloys has good wear and corrosion resistance because of the presence of phases having high hardness and toughness. This coating is widely used in various industries (Savrai et al. 2016). However, the
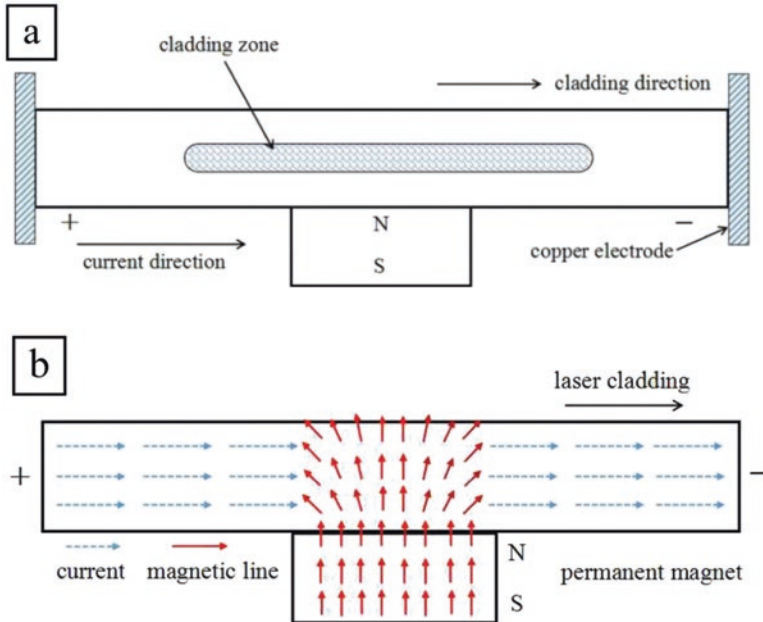
Fig. 11.17 Schematic of (**a**) laser cladding under electromagnetic field and (**b**) direction of magnetic and electric field (Zhai et al. 2019c)

presence of a variety of alloying elements in the coating can form a variety of solidification morphologies, and this may cause uneven distribution of hard phases in the matrix leading to the formation of cracks and subsequent reduction in service life of the cladded workpiece. Zhai et al. (2019c) studied the effects of electromagnetic field on microstructure, dilution, microhardness, and corrosion resistance on laser cladding of Ni-Cr-B-Si coating. A combination of four different magnetic field intensities and DC currents was tried out as given in Table 11.4, and corresponding cross-sectional SEM morphologies of the clad bead are presented in Fig. 11.19. Dilution was found to be the least under type 2 condition. Under only magnetic flux, the molten pool experiences Lorentz force directed against the fluid flow (Fig. 11.19b) which generates a decelerating flow in the molten pool. This also reduces the drag force of the fluid toward the cladding direction. Therefore, steady magnetic field is able to suppress the convection movement of the high-temperature molten material flowing into the bottom of the melt pool. As a result, because of less heat input at the molten pool and substrate interface, the penetration depth of the clad bead for type 2 condition is the least among all. With the introduction of electric field in type 3 condition, dilution increases. The presence of electric field decreases free electron density leading to decrease in conductivity of the metal and increase in electrical resistivity. Now, absorptivity of material (A) is related to electrical resistivity (ρ) according to Hagen-Rubens equation: $A = k \ (\rho/\lambda)^{1/2}$, where k = constant value of 0.365 and λ = wavelength of incident laser beam (Zhang et al. 2008c). Therefore,

Fig. 11.18 Schematic showing force analysis diagram of a point in molten pool; (**a**) without any magnetic and electric field, (**b**) with only magnetic field, and (**c**) with electromagnetic field (Zhai et al. 2019c)
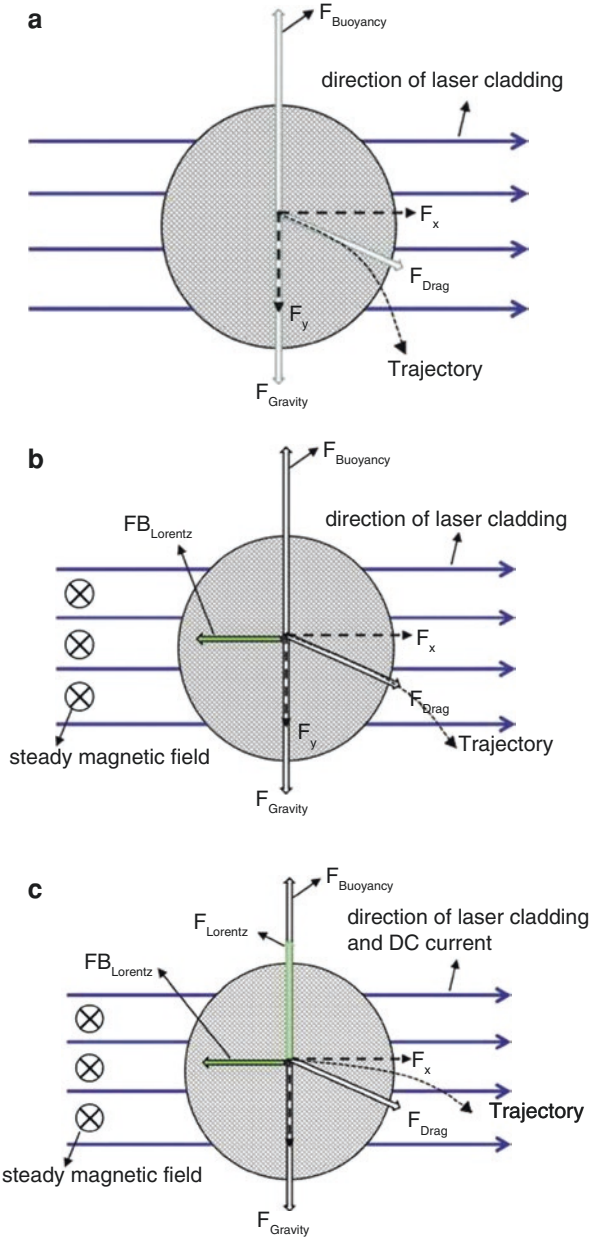

Table 11.4 Combination of different magnetic field intensities and DC currents (Zhai et al. 2019c)

	Type 1	Type 2	Type 3	Type 4
Magnetic field intensity [T]	0	0.2	0.2	0.2
DC current (A)	0	0	300	500
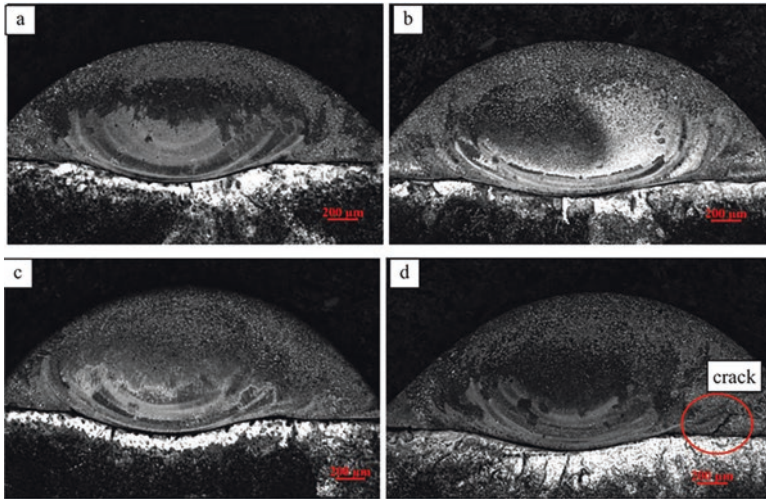
Fig. 11.19 Cross-sectional SEM morphologies of the clad bead of Ni-Cr-B-Si coating under (**a**) type 1, (**b**) type 2, (**c**) type 3, and (**d**) type 4 condition (Zhai et al. 2019c)

under type 3 condition, laser beam gets absorbed more, and consequently higher heat input leads to increase in substrate melting leading to higher dilution. Further increase in electric field (type 4 condition) causes cracks near the interface between clad layer and substrate. Increased electric field causes an increase in electromagnetic force in the upward direction (Fig. 11.19d). Once the solidification process begins, dendritic structure starts growing from the substrate which is at a relatively low temperature and forms interconnected network inside the molten pool material. As a result, molten liquid entrapped inside the dendritic network cannot be replaced by the external liquid. With increase in electromagnetic force, this entrapped liquid experiences greater upward thrust which in turn increases stress action when the solidification takes place and leads to cracking at the interface.

Zhai et al. (2019a, b) reported in the presence of alternating current, cracks can be minimized in the Ni-Cr-B-Si clad bead, as shown in Figs. 11.20 and 11.21. Diffusion of particular alloying elements inside molten pool can be controlled by using electromagnetic field. It was reported that magnetic field has effects on the diffusion of atoms in the material (Zhai et al. 2019c) following the Arrhenius equation $D = D_o \exp.(-Q/RT)$ where D = diffusion coefficient, D_o = frequency factor, R = gas constant, T = absolute temperature in Kelvin, and Q = activation energy. The factor D_o is smaller in the presence of a magnetic field, while the change in Q is negligible (Chen et al. 2016). As discussed earlier, steady magnetic field suppresses convective movement of the molten pool and thus hinders diffusion of elements leading to its accumulation and concentration. This leads to accumulation of chromium boride (CrB) phase as evident from Fig. 11.22b. With further introduction of electric field, the molten pool experiences a constant upward thrust due to electromagnetic force, and this promotes diffusion of elements to the upper part of the
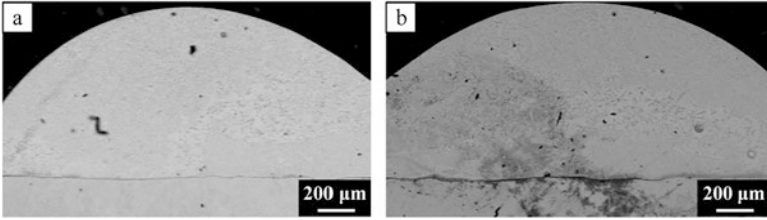
Fig. 11.20 SEM cross-sectional view of Ni-Cr-B-Si clad bead (**a**) with and (**b**) without alternating current (Zhai et al. 2019a)
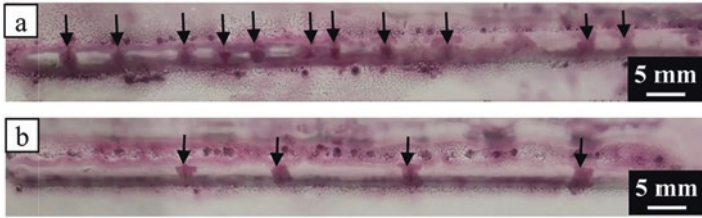

Fig. 11.21 Number of cracks in Ni-Cr-B-Si clad bead (**a**) with and (**b**) without alternating current (Zhai et al. 2019a)
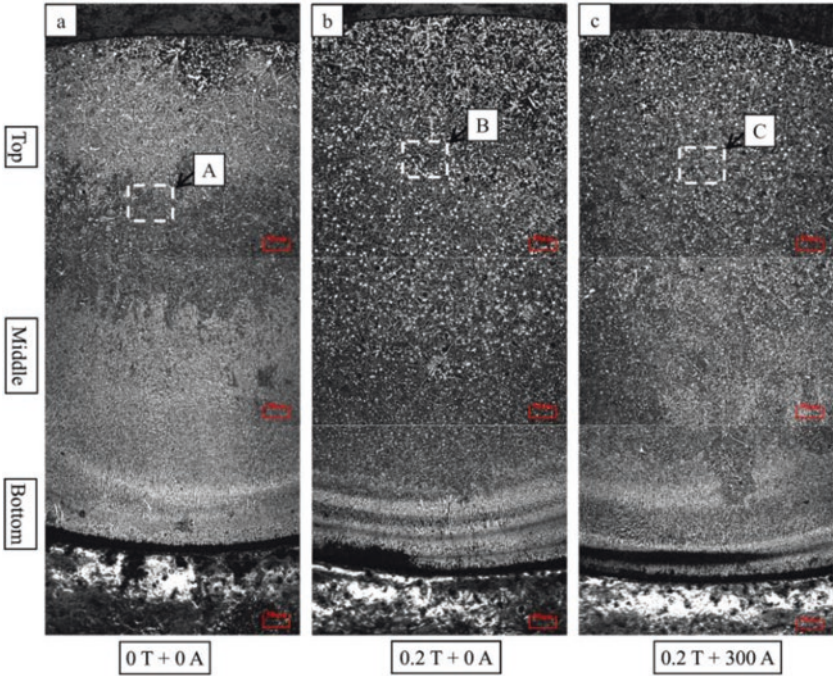

Fig. 11.22 SEM cross-sectional view of Ni-Cr-B-Si clad bead under (**a**) type 1, (**b**) type 2, and (**c**) type 3 condition; black spots contain relatively large Cr, and white color masses are CrB (Zhai et al. 2019c)

molten pool leaving relatively less elements at the middle of the clad bead. This observation can be visualized in Fig. 11.22c. Also, different morphologies of CrB are presented in Fig. 11.23 under different electromagnetic conditions. CrB having very high hardness in the range of 700 $HV_{0.2}$–1000 $HV_{0.2}$, its presence in a large number for type 2 (increase in microhardness at the bottom of the clad bead in this case may be noted) and type 3 condition increases hardness significantly, as shown in Fig. 11.24. Similar results on microhardness and corrosion resistance have also been reported by Zhai et al. (2019a) under alternating current. They reported that under alternating electric field, it is possible to promote the formation of equiaxed grains than the dendritic structure. It has been reported in the literature (Räbiger et al. 2014; Liao et al. 2007) that the electric field can improve nucleation rate and grain refinement. When current density is in certain range, i.e., $J > 2 (A\Delta G)^{1/2}$, nucleation rate can be improved and grain refinement be realized (Chen et al. 2019). Due to the skin effect of alternating current, current tends to confine on the surface of the conductive melt, and since the solid resistivity is less than that of the melt, current passes through the solid phase preferentially also. Now due to the low temperature of the substrate, solidification of the melt pool begins at the bottom where the current concentrates (Fig. 11.25) and as a result the bottom of the clad bead experiences a larger current density. Increased current densities is linked to higher grain refinement and causes refinement in grains at the top and bottom of the clad bead more (Fig. 11.26). Grain refinement in the upper portion is also effected by the external environment leading to higher cooling rate. On the other hand, in the middle of the clad bead, the insufficient current density for grain refinement, Joule heating, and relatively slower cooling rates cause grain coarsening (Zhai et al. 2019c). Lu et al. (2019) studied the effect of stress distribution of the molten pool under both static and dynamic electromagnetic fields. It was found that the rotating fields have stronger ability to stabilize the stress field compared to static fields.

The above works illustrate the possibility to modify/control grain size and distribution of alloying elements, increase microhardness and corrosion resistance, and reduce the number of cracks and dilution in laser cladding of Ni-based coating by means of external magnetic or electric or combination of both either in static or rotating condition.

11.4.2   *Ultrasonic Vibration-Assisted Laser Cladding Process*

In the presence of ultrasonic vibration, periodical positive-negative pressure waves get generated in the molten pool. This causes two major nonlinear actions, namely, acoustic streaming and cavitation. In case of acoustic streaming, there is a steady flow that is driven by momentum transfer due to the absorption of multiple acoustic oscillations in the liquid molten material. On the other hand, cavitation is a phenomenon which causes generation of tiny bubbles/cavities and its subsequent growth, pulsation, and collapse in the liquid molten material. These two actions generate agitation in the melt pool and cause different direct and ultimate influences (Cong
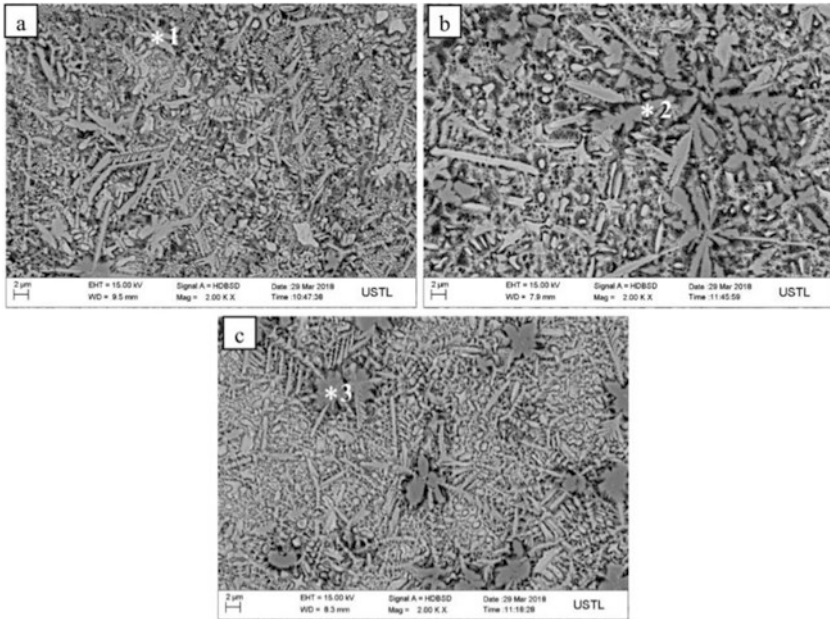
Fig. 11.23 Chromium boride (CrB) having different morphologies under (**a**) type 1, (**b**) type 2, and (**c**) type 3 condition (Zhai et al. 2019c)
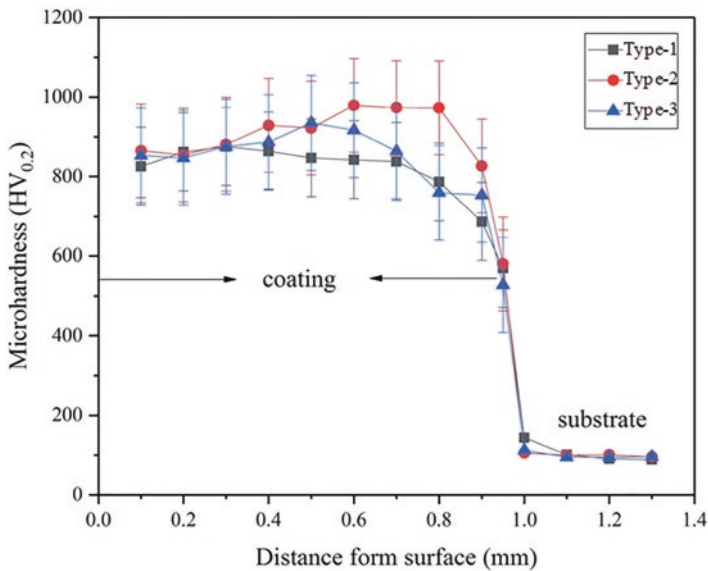

Fig. 11.24 Variation in microhardness under different electromagnetic conditions (Zhai et al. 2019c)
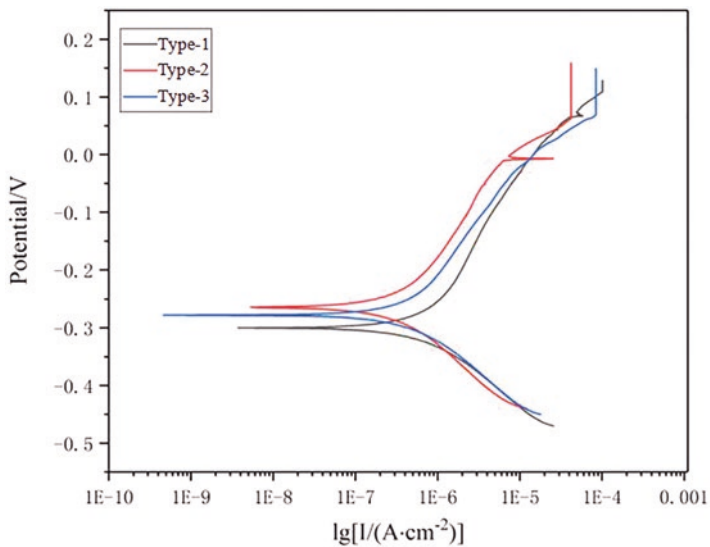
Fig. 11.25 Linear polarization curve of the Ni-Cr-B-Si clad bead with and without electromagnetic clad bead (Zhai et al. 2019c)
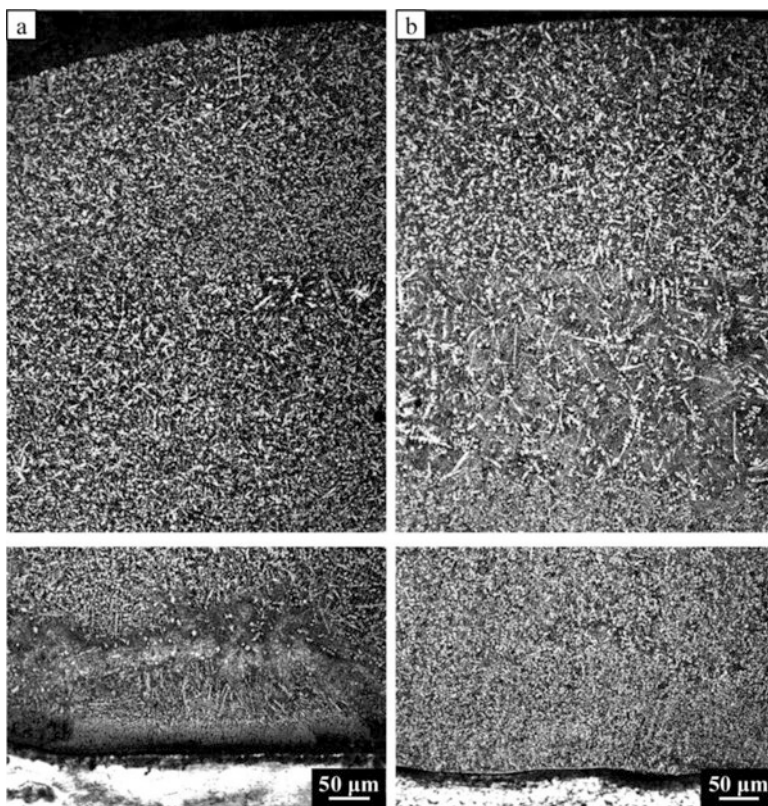

Fig. 11.26 SEM cross-sectional view of Ni-Cr-B-Si clad bead (**a**) with and (**b**) without the alternating electric field (Zhai et al. 2019a)
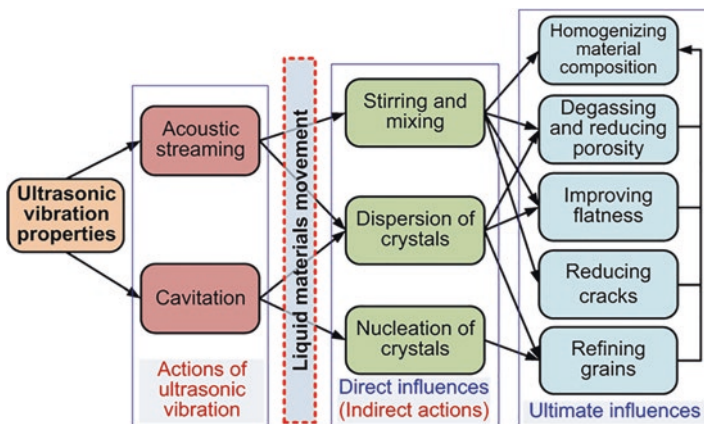
Fig. 11.27 Actions and influences of ultrasonic vibration in ultrasonic vibration-assisted melting in metal solidification processes (Cong and Ning 2017)

and Ning 2017) as summarized in Fig. 11.27. Under these influences, ultrasonic vibrations could refine grains, homogenize and redistribute alloying particles, and reduce pores and segregation; combined effect of all these can enhance mechanical and corrosion properties of the deposition. Parameters related to ultrasonic vibration-assisted melting process, i.e., DMLD, laser surface remelting, etc., include direction of vibration, ultrasonic power, frequency (commonly used 20–40 kHz), and amplitude (10–150 μm) of ultrasonic vibration, laser power, scan speed, laser spot diameter, number of layers, etc. Although various effects of ultrasonic vibration on clad quality of different materials are available in literature, only Ni-based alloy and coating are discussed here. In the next section, effects of ultrasonic vibration on grain size, porosity, segregation, and microhardness are discussed by taking an example of fabrication of IN 718 test coupons using laser-engineered net shaping (LENS) process.

Porosity is a major issue in laser cladding process. It causes reduction in fatigue life. Mostly, entrapment of gas bubbles triggers the formation of pores in the molten tracks. Acoustic streaming and cavitation effect in case of ultrasonic vibration-assisted processing generates radiation pressure waves to change the interaction between metallic liquid and entrapped gas bubbles, subsequently leading to collapse of gas-evolved pores. This is illustrated in Fig. 11.28 which shows a significant reduction in the pores in case of ultrasonic vibration-assisted processing.

Acoustic streaming and cavitation effect during microstructure formation causes formation of a large number of grain nucleation sites which results in refinement in grains (Fig. 11.29). It is well established that the grain refinement significantly increases strength and hardness of the material and a more well-arranged and homogenous microstructure reduces residual stresses caused during rapid solidification of the molten material (Furuhara and Maki 2001; Abramov 1987). The Hall-Petch equation suggests that the microhardness of any material is correlated to the
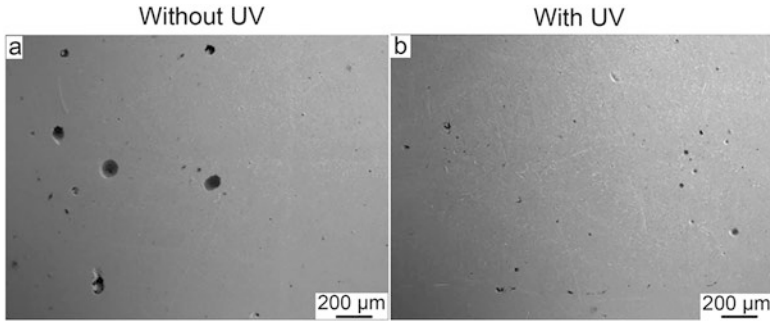
Fig. 11.28 Reduction in pores in case of ultrasonic vibration-assisted processing of IN 718 using LENS process (Ning et al. 2017)
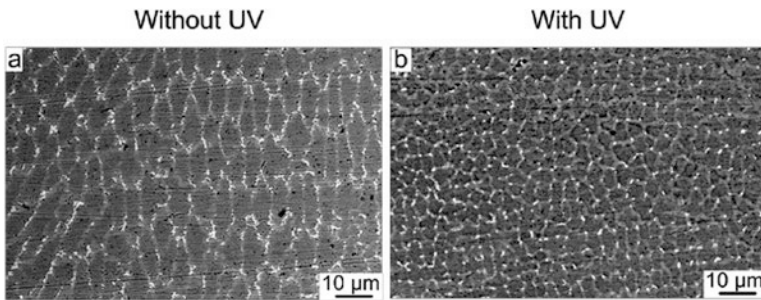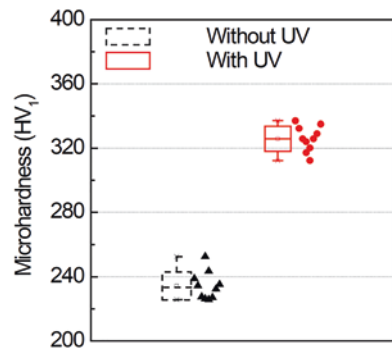

Fig. 11.29 Reduction in grain size in case of ultrasonic vibration-assisted processing of IN 718 using LENS process (Ning et al. 2017)

Fig. 11.30 Increase in microhardness value in case of ultrasonic vibration-assisted processing of IN 718 using LENS process (Ning et al. 2017)

reciprocal root of the grain size. Therefore, with the decrease in grain size, it is expected to increase the microhardness value for ultrasonic vibration-assisted processing, for example, as shown in Fig. 11.30.

As discussed earlier, one of the major problems in Ni-based superalloy cladding is the segregation of Laves phases which is detrimental to mechanical and corrosion

Fig. 11.31 Fragmentation of Laves phases in case of ultrasonic vibration-assisted processing of IN 718 using LENS process (Ning et al. 2017)
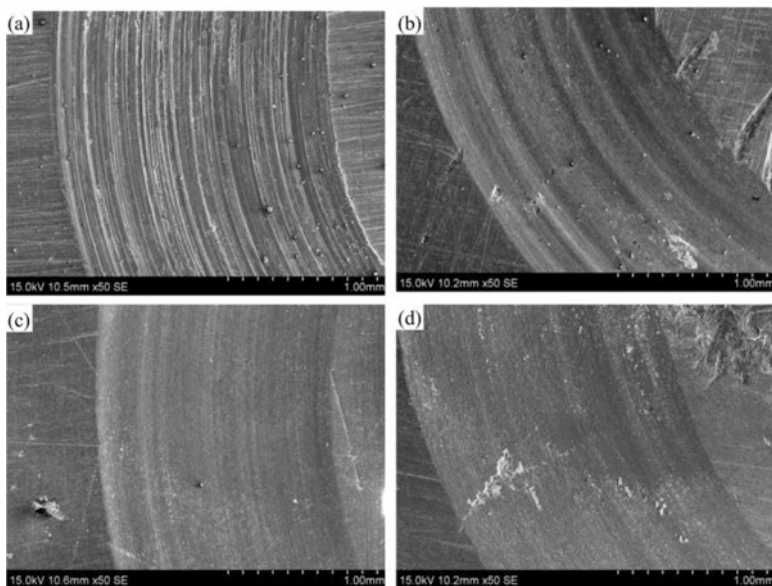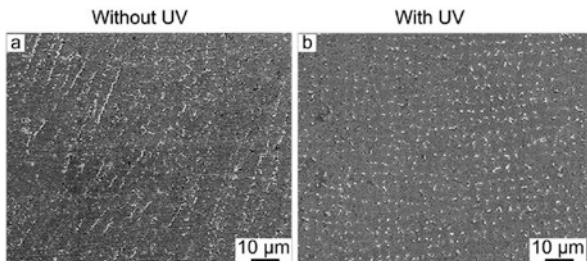

Fig. 11.32 Worn surfaces of laser-cladded WC-Ni coating (**a**) without ultrasonic vibration (**b–d**) and with ultrasonic vibration (Li et al. 2019)

properties due to the brittle nature of these phases. During ultrasonic vibration-assisted processing, radiation pressure of the acoustic field makes the solid-liquid interface unstable. These lead to the fragmentation of long bar-shaped Laves phases into small globular ones uniformly distributed over the matrix (Fig. 11.31). Several researchers (Li et al. 2016; Li et al. 2019) have reported increased microhardness and wear resistance in case of ultrasonic vibration-assisted laser cladding of Ni-ceramic coating (Fig. 11.32). Micro-vibration during laser cladding could make better mechanical stirring effect for mixing hard phases in the matrix resulting in more uniform microstructure.

Improvement in corrosion properties of laser cladding assisted by mechanical vibration has been realized. Liu et al. (2015) reported improved corrosion resistance (Fig. 11.33) of Ni60CuMoW laser-cladded coating. Micro-mechanical vibration
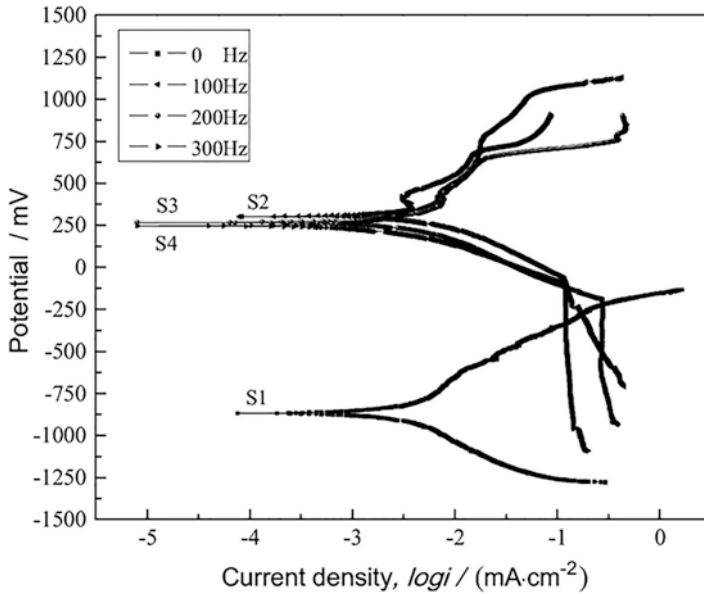
Fig. 11.33 Polarization curves of cladding Ni60CuMoW coatings with or without ultrasonic vibration in 3.5% NaCl solution (Liu et al. 2015)

improved mean particle size of the hard phases and maintained uniformity in micro-structure during melting and solidification process. Uniform microstructure, high surface density, increase in Cr content in carbides, and interface bonding strength between hard phase particles and the matrix are found to be the major driving fac-tors in improving the corrosion resistance of ultrasonic vibration-assisted deposited coating.

These studies illustrate the possibility of controlling the grain size, segregation of Laves phases, reduction of porosity, improvement of microhardness, wear, and corrosion resistance in laser cladding of Ni-based alloy using ultrasonic vibration for better mechanical and corrosion properties.

11.4.3   Rare Earth Elements Added in Nickel Coatings

Rare earth elements comprise of 15 lanthanides with atomic numbers ranging from 57 to 71 with exceptions of scandium and yttrium. The presence of these rare earth elements having large atomic radius in the solid solution causes substantial lattice distortion increasing the total energy of the system (Wang et al. 2001). These rare earth elements are mostly stable near the grain boundaries. Therefore, during the solidification process, they try to segregate at the grain boundary. This causes a drag effect on the growing crystal or grain limiting its size along and favoring formation

of new nucleation sites with time or decrease in temperature resulting not only in the refinement of microstructure but also in controlling the segregation and inhomogeneity in microstructure. Further, this results in increased area of the grain boundary restricting the crack propagation. The problem of cracks is more predominant in case of nickel-based ceramic coating due to large variation in the thermos-physical properties of the material being cladded. Li et al. (2017) studied the influence of the addition of La_2O_3 on crack susceptibility during laser cladding of Ni-based ceramic composite, and it was found that an addition of 0.6–0.8% of La_2O_3 could bring down the crack susceptibility to zero. In addition to refining the microstructure, rare earth elements also act as surfactants reducing the surface tension and interfacial energy between the crystal nucleus and the melt leading to increased wettability between the metal matrix and the ceramic phase favoring formation of shell-core structure improving the mechanical property of the coating (Niu and Chang 1999; Zhao et al. 2020). Rare earth elements also increase the latent heat of melting of the cladding materials, instigating increase in solidus temperature, and decrease liquid temperature leading to shorter solidification time resulting in finer microstructure. Further, this also limits diffusion of substrate materials into the clad material, thereby controlling the dilution. As discussed, rare earth elements reduce the solid-liquid interfacial energy, potentially reducing the Gibbs free energy required for the formation of nucleus promoting more number of nuclei. Also, the rare earth particles in some cases themselves act as nucleating sites. Therefore, the combination of drag effect, reduced solid-liquid interfacial energy, and action as heterogeneous nucleation sites results in refinement of microstructure and improved surface and mechanical characteristics. Figure 11.34 shows the effect of the addition of 6% La_2O_3 on the microstructure during laser cladding of Ni-based alloy powder (Li et al. 2017). It can be clearly observed that the addition of rare earth oxide resulted in refinement as well as the randomization of microstructure without any directionality as compared to that of cladding pure Ni-based alloy powder. Further, Li et al. (2017) also reported an increase in corrosion resistance along with the grain refinement. In addition to their chemical behavior, the particle size of the rare earth elements used also plays a critical role in controlling the microstructure as well as the surface properties. Zhang et al. (2008b) investigated the effect of the addition of nano- and micro-sized Sm_2O_3 on the microstructure and corrosive properties of laser-cladded NBA powder (NiSp475). Figure 11.35 (Zhang et al. 2008b) shows the morphology of sample surface tested for corrosion. In Fig. 11.35a, it can be observed that NBA coating without any rare earth oxide suffered severe corrosion of dendrite with significant pitting, whereas the samples with addition of 1.5% Sm_2O_3 showed a minimum corrosion with nano-sized particles (Fig. 11.35c) offering better corrosion resistance than the micro-sized particles (Fig. 11.35b). In addition to microstructure refinement and corrosion resistance, addition of rare earth materials was also reported to increase hardness and wear resistance of the coatings due to the refined microstructure with good wetting characteristics (Wang et al. 1977, 2001; Zhang et al. 2008a).
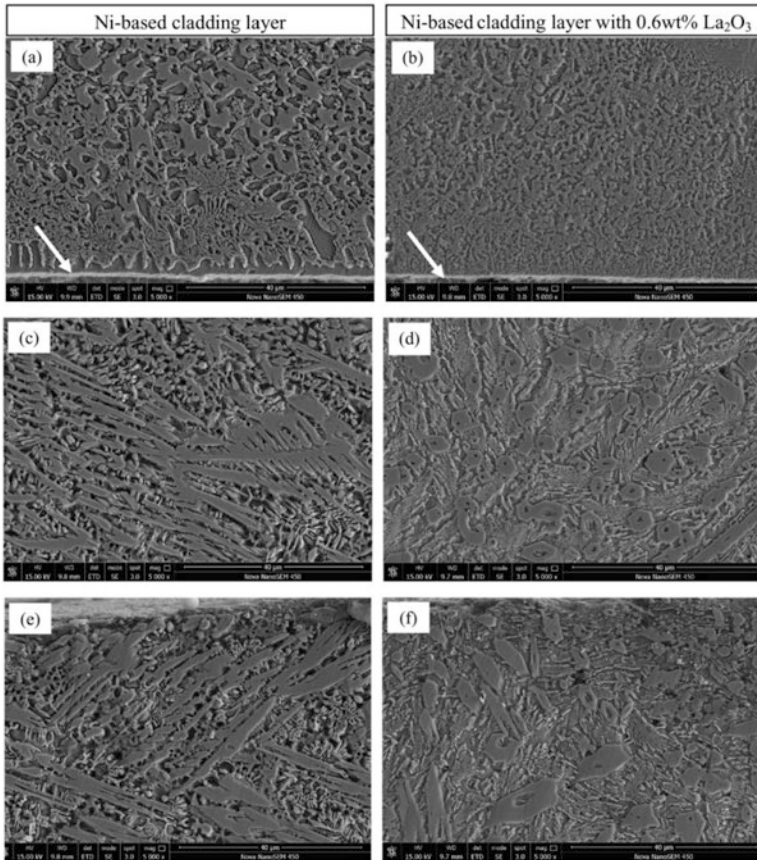
Fig. 11.34 Effect of La$_2$O$_3$ addition on microstructure refinement in Ni-based alloy powder: (**a**, **b**) bottom region, (**c**, **d**) middle region, and (**e**, **f**) upper region (Li et al. 2017)

11.5 Metal Matrix Composite Coatings of Nickel-Based Alloys

Nickel-based superalloys are generally good candidates for the development of corrosive coatings. However, they suffer from relatively poor wear resistance compared to several other superalloys like Stellite, etc. Therefore, with the increasing demand for enhanced component life, nickel-based metal matrix composite (MMC) coatings are becoming popular in almost every industry including aerospace, automobile, mining and mineral industry, etc., for armoring over turbine blade tips, pistons, valves, cylinders, drilling tools, etc., where the failure of mechanical components is generally caused by wear, erosion, and corrosion at the surface. However, these ceramic coatings experience unique problem of cracking due to rapid solidification and residual stresses, compositional changes due to their dissolution in metal matrix
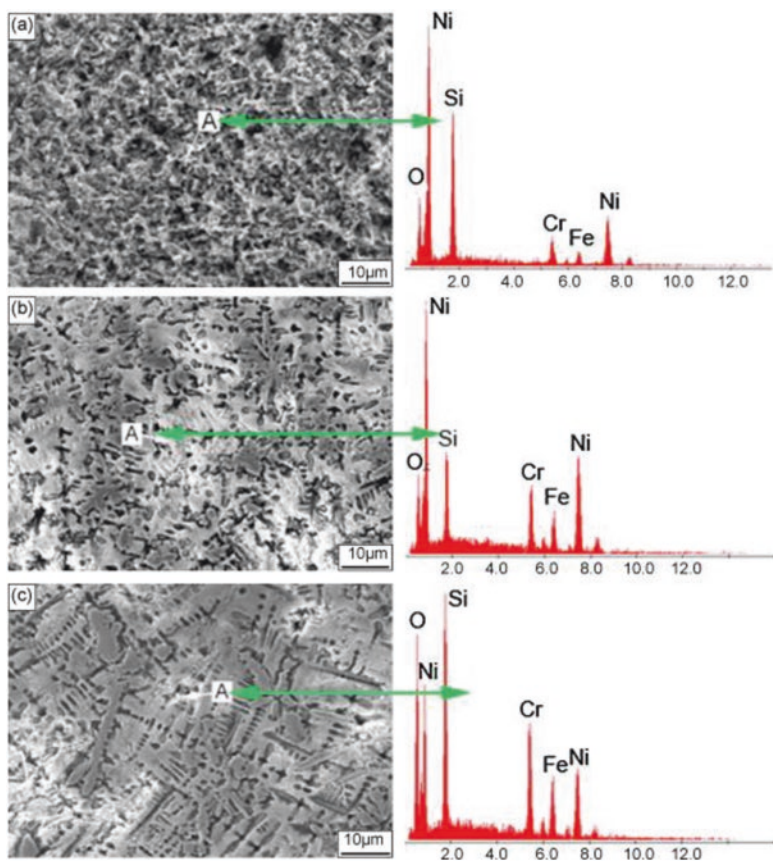
Fig. 11.35 Electrochemical corrosion morphology of the coatings: (**a**) 0% Sm_2O_3; (**b**) 1.5% m-Sm_2O_3; (**c**) 1.5% n-Sm_2O_3 (Zhang et al. 2008b)

affecting the corrosion and mechanical properties, and nonuniform distribution due to differences in their physical properties. Therefore, it is important to understand the influence of process parameters on these aspects.

As discussed in the previous section, one of the major reasons for the failure of a coating or component is the separation of the two phases upon application of load. Therefore, it is essential to establish a tailoring joint between the ceramic particles and the metal matrix. Muvvala et al. (2017a) investigated the effect of various process parameters on the tailoring of WC ceramic particles with the Inconel 718 metal matrix. Apart from the process parameters, WC wetting or tailoring is found to be a function of molten pool lifetime, as shown in Fig. 11.36. It can be observed that there is an optimum range of melt pool lifetime for the proper WC tailoring with the matrix. For a relatively short molten pool lifetime, the wetting or bonding between WC particles and the metal matrix is very poor with a distinct boundary between them. However, with increase in molten pool lifetime beyond a limit (above ~0.68 s),
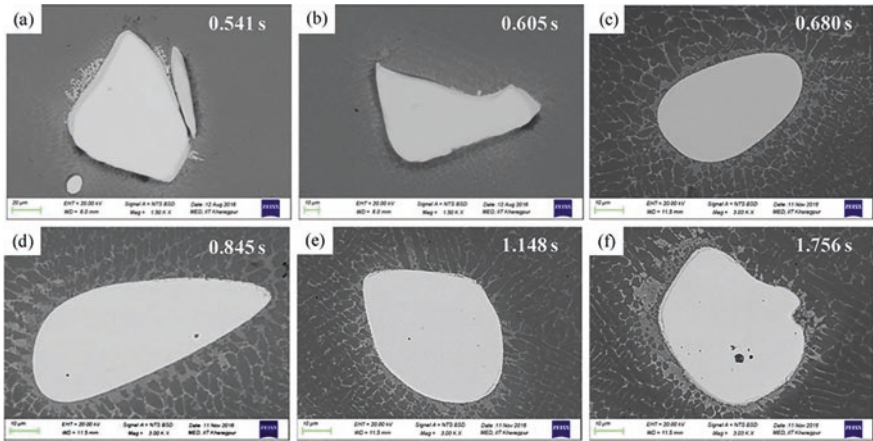
Fig. 11.36 Variation in wetting condition of ceramic particles with laser scan speed of (**a**) 1200 mm/min, (**b**) 1000 mm/min, (**c**) 800 mm/min, (**d**) 600 mm/min, (**e**) 400 mm/min, and (**f**) 200 mm/min (1200 W) (Muvvala et al. 2017a)
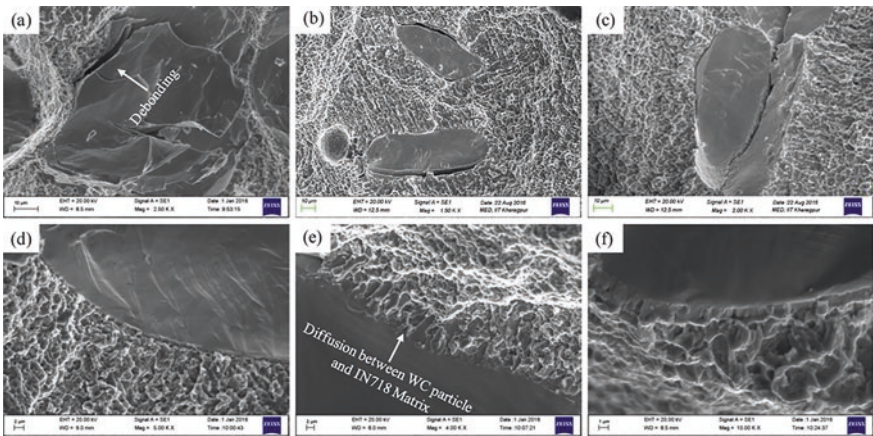

Fig. 11.37 Fracture surfaces of clad layer showing the bonding condition between the ceramic particles and the metal matrix deposited with 1200 W laser power and scan speed of (**a**) 1200 mm/min, (**b**) 1000 mm/min, (**c**) 800 mm/min, (**d**) 600 mm/min, (**e**) 400 mm/min, and (**f**) 200 mm/min (Muvvala et al. 2017a)

a clear diffusion bonding is visible tailoring the WC particles with the matrix. Figure 11.37 shows the effect of poor wetting on the fracture properties of the nickel-based coatings. A distinct delamination between the ceramic particles and the matrix is visible under the application of load. Thus, these weak interfaces act as crack initiation points resulting in premature failure of the coating under the applied load in the operation condition. Therefore, it is very essential to ensure wettability

and tailoring in ceramic MMC by controlling the process parameters to provide sufficiently slow cooling rate or long melt pool lifetime.

However, too long a melt pool lifetime could be detrimental to the quality of coating due to various effects depending on the properties of ceramic particles being added in the Ni superalloy matrix. In the case of WC particles which have a density ~16.5 g/cm^3, almost twice that of Inconel 718 and most of the other nickel-based superalloys, they tend to sink in the molten pool (Fig. 11.38). This results in a graded WC particle concentration in the coating with fewer of them on the top surface with no improvement of wear characteristic of the Ni alloy coating (Fig. 11.39) (Muvvala et al. 2017a, Fernández et al. 2015).

In addition to the issue of particle sinking, dissociation of ceramic particles is also one of the major concerns for longer melt pool lifetime in nickel-based ceramic composite coating. Figure 11.40 shows the effect of longer molten pool lifetime on the decomposition and resulting mechanical properties of the Inconel/TiC composite coating. For relatively long molten pool lifetimes, the decomposition of TiC
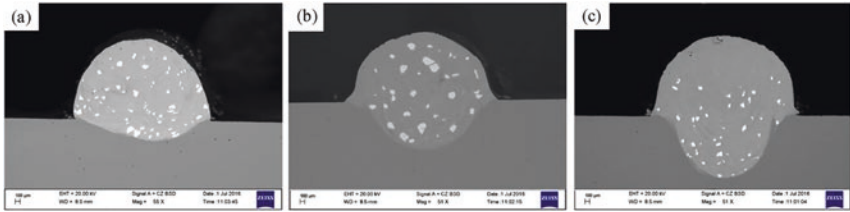

Fig. 11.38 Distribution of WC particles in clad layer: (**a**) 600 mm/min, (**b**) 400 mm/min, and (**c**) 200 mm/min (Muvvala et al. 2017a)
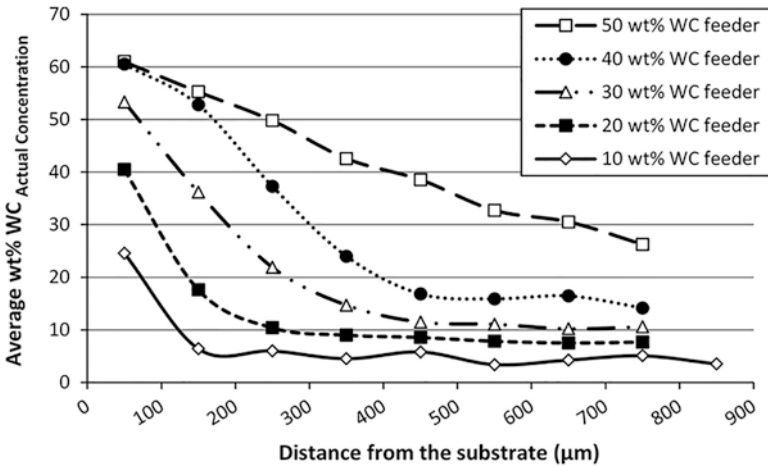

Fig. 11.39 Average wt% WC$_{actual\ concentration}$ versus the distance to the substrate in the cross section of a NiCrBSi coating for different wt% WC$_{feeder\ concentration}$ (Fernández et al. 2015)
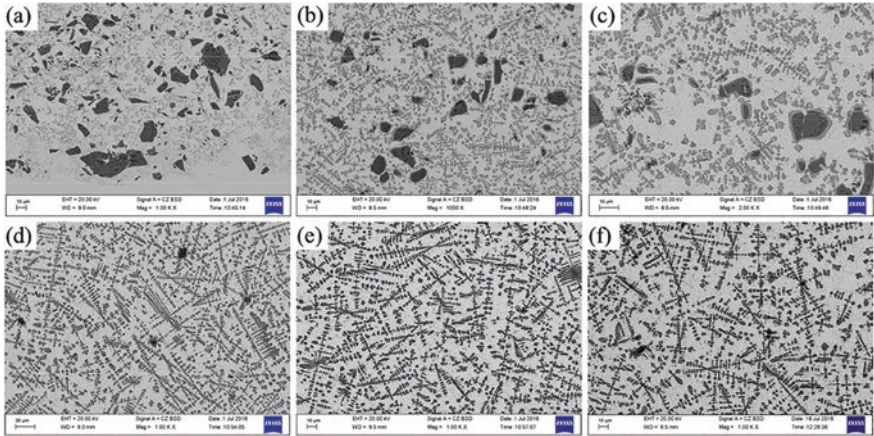
Fig. 11.40 Variation in microstructure with molten pool lifetime: (**a**) 0.281 s, (**b**) 0.3 s, (**c**) 0.429 s, (**d**) 0.487 s, (**e**) 0.899 s, and (**f**) 1.336 s (Muvvala et al. b)
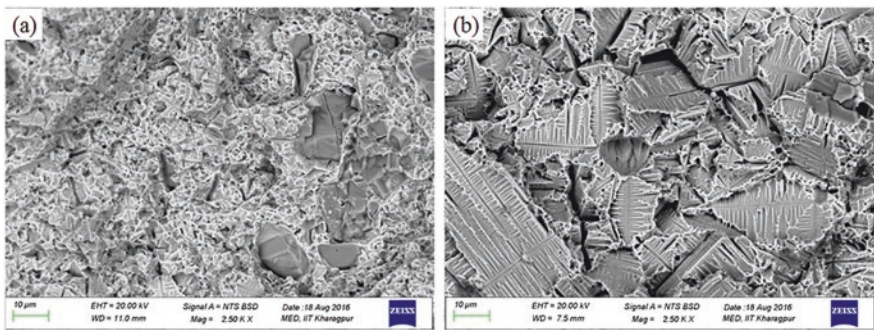

Fig. 11.41 Fracture surface of samples cladded at 1200 W laser power and (a) 1200 mm/min and (b) 400 mm/min scan speed (Muvvala et al. 2017b)

becomes severe resulting in microstructure with fully grown ceramic dendritic structure which essentially results in the brittle fracture of the coating both under wear test and tensile loading as reported by Muvvala et al. (2017b) and Liu and Shin (2017) and evident from Fig. 11.41 (Muvvala et al. 2017b).

11.6   Conclusion

Nickel-based superalloys find a wide range of applications in the field of aerospace, nuclear power plants, and many other industries owing to its excellent properties at both room and elevated temperatures. With the advancement in additive

manufacturing technology, fabrication or refurbishment of components or development of protective coatings based on nickel-based alloys also took a steep leap forward. However, they suffer from elemental segregations during the laser cladding process which are detrimental to both the surface and bulk mechanical properties. Optimizing or limiting the segregation with respect to process parameters is feasible, and this has been correlated with the cooling rate/melt pool lifetime in laser cladding process. In fact, cooling rate is found to be such a parameter which dictates the quality of the coating irrespective of process parameters and laser cladding system. In addition to the process parameters and the resulting cooling rates, external agitation of molten pool through electromagnetic field and ultrasonic vibrations and addition of rare earth elements are found to control the segregations improving the mechanical and surface properties. Further, the properties of nickel-based ceramic coating are also found possible to be controlled with the cooling rate.

References

Abramov, O. V. (1987). Action of high intensity ultrasound on solidifying metal. *Ultrasonics, 25*(2), 73–82. https://doi.org/10.1016/0041-624X(87)90063-1.

Caiazzo, F. (2018). Laser-aided directed metal deposition of Ni-based superalloy powder. *Optics and Laser Technology, 103*, 193–198. https://doi.org/10.1016/j.optlastec.2018.01.042.

Cemal, M., Cevik, S., Uzunonat, Y., & Diltemiz, F. (2012). ALLVAC 718 Plus™ superalloy for aircraft engine applications. In R. Agarwal (Ed.), *Recent advances in aircraft technology*. Eskisehir: InTech. https://doi.org/10.5772/38433.

Chen, R., Wang, C. M., Jiang, P., et al. (2016). Effect of axial magnetic field in the laser beam welding of stainless steel to aluminum alloy. *Materials and Design, 109*, 146–152. https://doi.org/10.1016/j.matdes.2016.07.064.

Chen, Z. X., Ding, H. S., Chen, R. R., et al. (2019). An innovative method for the microstructural modification of TiAl alloy solidified via direct electric current application. *Journal of Materials Science and Technology, 35*(1), 23–28. https://doi.org/10.1016/j.jmst.2018.06.016.

Chlebus, E., Gruber, K., Kuźnicka, B., Kurzac, J., & Kurzynowski, T. (2015). Effect of heat treatment on the microstructure and mechanical properties of Inconel 718 processed by selective laser melting. *Materials Science and Engineering A, 639*, 647–655. https://doi.org/10.1016/j.msea.2015.05.035.

Cong, W., & Ning, F. (2017). A fundamental investigation on ultrasonic vibration-assisted laser engineered net shaping of stainless steel. *International Journal of Machine Tools and Manufacture, 121*(2017), 61–69. https://doi.org/10.1016/j.ijmachtools.2017.04.008.

Dinda, G. P., Dasgupta, A. K., & Mazumder, J. (2009). Laser aided direct metal deposition of Inconel 625 superalloy: Microstructural evolution and thermal stability. *Materials Science and Engineering A, 509*, 98–104. https://doi.org/10.1016/j.msea.2009.01.009.

DuPont, J. N., Lippold, J. C., & Kiser, S. D. (2009). *Welding metallurgy and weldability of nickel-base alloys*. Hoboken: Wiley.

Eliaz, N., Shemesh, G., & Latanision, R. M. (2002). Hot corrosion in gas turbine components. *Engineering Failure Analysis, 9*, 31–43. https://doi.org/10.1016/S1350-6307(00)00035-2.

Fernández, M. R., García, A., Cuetos, J. M., González, R., Noriega, A., & Cadenas, M. (2015). Effect of actual WC content on the reciprocating wear of a laser cladding NiCrBSi alloy reinforced with WC. *Wear, 324–325*, 80–89. https://doi.org/10.1016/j.wear.2014.12.021.

Furuhara, T., & Maki, T. (2001). Variant selection in heterogeneous nucleation on defects in diffusional phase transformation and precipitation. *Materials Science and Engineering A, 312*(1), 145–154. https://doi.org/10.1016/S0921-5093(00)01904-3.

Gopinath, M., Karmakar, D. P., & Nath, A. K. (2017). Monitoring of molten pool thermal history and its significance in laser cladding process. *Proceedings of the ASME 2017 12th international manufacturing science and engineering conference collocated with the JSME/ASME 2017 6th international conference on materials and processing. Volume 2: Additive manufacturing; Materials. Los Angeles, California, USA*. V002T01A041. https://doi.org/10.1115/MSEC2017-2657.

Inconel 625 data sheet. https://www.specialmetals.com/assets/smc/documents/alloys/inconel/inconel-alloy-625.pdf

Kang, N., Mansori, M. E., Guittonneau, F., Liao, H., Fu, Y., & Aubry, E. (2018). Controllable mesostructure, magnetic properties of soft magnetic Fe-Ni-Si by using selective laser melting from nickel coated high silicon steel powder. *Applied Surface Science, 455*, 736–741. https://doi.org/10.1016/j.apsusc.2018.06.045.

Kou, S. (2002). *Welding metallurgy* (2nd ed.). Hoboken: John Wiley & Sons Inc.

Leary, M., Mazur, M., Williams, H., Yang, E., Alghamdi, A., Lozanovski, B., et al. (2018). Inconel 625 lattice structures manufactured by selective laser melting (SLM): Mechanical properties, deformation and failure modes. *Materials and Design, 157*, 179–199. https://doi.org/10.1016/j.matdes.2018.06.010.

Li, M., Han, B., Wang, Y., Song, L., & Guo, L. (2016). Investigation on laser cladding high-hardness nano-ceramic coating assisted by ultrasonic vibration processing. *Optik, 127*, 4596–4600. https://doi.org/10.1016/j.ijleo.2016.01.194.

Li, M., Han, B., Wang, Y., & Pu, K. (2017). Effects of La_2O_3 on the microstructure and property of laser cladding Ni-based ceramic coating. *Optik, 130*, 1032–1037. https://doi.org/10.1016/j.ijleo.2016.11.111.

Li, C., Zhang, Q., Wang, F., Deng, P., Lu, Q., Zhang, Y., Li, S., Ma, P., Li, W., & Wang, Y. (2019). Microstructure and wear behaviors of WC-Ni coatings fabricated by laser cladding under high frequency micro-vibration. *Applied Surface Science, 485*, 513–519. https://doi.org/10.1016/j.apsusc.2019.04.245.

Liao, X. L., Zhai, Q. J., Luo, J. L., et al. (2007). Refining mechanism of the electric current pulse on the solidification structure of pure aluminium. *Acta Materialia, 55*(9), 3103–3109. https://doi.org/10.1016/j.actamat.2007.01.014.

Liu, S., & Shin, Y. C. (2017). The influences of melting degree of TiC reinforcements on microstructure and mechanical properties of laser direct deposited Ti6Al4V-TiC composites. *Materials and Design, 136*, 185–195. https://doi.org/10.1016/j.matdes.2017.09.063.

Liu, X. H., Ji, S. W., Jiang, Y. H., et al. (2013). Microstructure and property of Fe60 composite coatings by rotating magnetic field auxiliary laser cladding. *Chinese Journal of Lasers, 40*(1), 115–120.

Liu, H., Xu, Q., Wang, C., & Zhang, X. (2015). Corrosion and wear behavior of Ni60CuMoW coatings fabricated by combination of laser cladding and mechanical vibration processing. *Journal of Alloys and Compounds, 621*, 357–363. https://doi.org/10.1016/j.jallcom.2014.10.030.

Lu, Y., Sun, G., Wang, Z., Zhang, Y., Su, B., Feng, A., & Ni, Z. (2019). Effects of electromagnetic field on the laser direct metal deposition of austenitic stainless steel. *Optics and Laser Technology, 119*, 105586. https://doi.org/10.1016/j.optlastec.2019.105586.

Luo, S., Huang, W., Yang, H., Yang, J., Wang, Z., & Zeng, X. (2019). Microstructural evolution and corrosion behaviors of Inconel 718 alloy produced by selective laser melting following different heat treatments. *Additive Manufacturing, 30*, 100875. https://doi.org/10.1016/j.addma.2019.100875.

Marchese, G., Parizia, S., Rashidi, M., Saboori, A., Manfredi, D., Ugues, D., Lombardi, M., Hryha, E., & Biamino, S. (2020). The role of texturing and microstructure evolution on the tensile behavior of heat-treated Inconel 625 produced via laser powder bed fusion. *Materials Science and Engineering A, 769*, 138500. https://doi.org/10.1016/j.msea.2019.138500.

Ming, X. L., Chen, J., Tan, H., Yang, H. O., & Lin, X. (2015). Research on persistent fracture mechanism of laser forming repaired GH4169 superalloy. *Chin. J. Lasers., 42*, 0403005.

Moussaoui, K., Rubio, W., Mousseigne, M., Sultan, T., & Rezai, F. (2018). Effects of selective laser melting additive manufacturing parameters of Inconel 718 on porosity, microstructure and mechanical properties. *Materials Science and Engineering A, 735*, 182–190. https://doi.org/10.1016/j.msea.2018.08.037.

Muvvala, G., Karmakar, D. P., & Nath, A. K. (2017a). Monitoring and assessment of tungsten carbide wettability in laser cladded metal matrix composite coating using an IR pyrometer. *Journal of Alloys and Compounds, 714*, 514–521. https://doi.org/10.1016/j.jallcom.2017.04.254.

Muvvala, G., Karmakar, D. P., & Nath, A. K. (2017b). Online assessment of TiC decomposition in laser cladding of metal matrix composite coating. *Materials and Design, 121*, 310–320. https://doi.org/10.1016/j.matdes.2017.02.061.

Muvvala, G., Karmakar, D. P., & Nath, A. K. (2017c). Online monitoring of thermo-cycles and its correlation with microstructure in laser cladding of nickel based super alloy. *Optics and Lasers in Engineering, 88*, 139–152. https://doi.org/10.1016/j.optlaseng.2016.08.005.

Nair, A. M., Muvvala, G., & Nath, A. K. (2019). A study on in-situ synthesis of TiCN metal matrix composite coating on Ti-6Al-4V by laser surface alloying process. *Journal of Alloys and Compounds, 810*, 151901. https://doi.org/10.1016/j.jallcom.2019.151901.

Ning, F., Hu, Y., Liu, Z., Cong, W., Li, Y., & Wang, X. (2017). Ultrasonic vibration-assisted laser engineered net shaping of Inconel 718 parts: A feasibility study. *Procedia Manufacturing, 10*, 771–778. https://doi.org/10.1016/j.promfg.2017.07.074.

Niu, H. J., & Chang, I. T. H. (1999). Selective laser sintering of gas and water atomized high speed steel powders. *Scripta Materialia, 41*(1), 25. https://doi.org/10.1016/s1359-6462(99)00089-5.

Oblak, J. M., Paulonis, D. F., & Duvall, D. S. (1974). Coherency strengthening in Ni base alloys hardened by DO22 γ″ precipitates. *Metallurgical Transactions, 5*, 143–153. https://doi.org/10.1007/BF02642938.

Odabasi, A., Unlu, N., Goller, G., & Eruslu, M. N. (2010). A study on laser beam welding (LBW) technique: Effect of heat input on the microstructural evolution of superalloy Inconel 718. *Metallurgical and Materials Transactions A: Physical Metallurgy and Materials Science, 41*, 2357–2365. https://doi.org/10.1007/s11661-010-0319-y.

Paul, C. P., Ganesh, P., Mishra, S. K., Bhargava, P., Negi, J., & Nath, A. K. (2007). Investigating laser rapid manufacturing for Inconel-625 components. *Optics and Laser Technology, 39*, 800–805. https://doi.org/10.1016/j.optlastec.2006.01.008.

Qiu, C., Chen, H., Liu, Q., Yue, S., & Wang, H. (2019). On the solidification behaviour and cracking origin of a nickel-based superalloy during selective laser melting. *Materials Characterization, 148*, 330–344. https://doi.org/10.1016/j.matchar.2018.12.032.

Räbiger, D., Zhang, Y. H., Galindo, V., et al. (2014). The relevance of melt convection to grain refinement in Al–Si alloys solidified under the impact of electric currents. *Acta Materialia, 79*, 327–338. https://doi.org/10.1016/j.actamat.2014.07.037.

Ramakrishnan, A., & Dinda, G. P. (2019). Direct laser metal deposition of Inconel 738. *Materials Science and Engineering A, 740–741*, 1–13. https://doi.org/10.1016/j.msea.2018.10.020.

Rao, G. A., Srinivas, M., & Sarma, D. S. (2004). Effect of thermomechanical working on the microstructure and mechanical properties of hot isostatically pressed superalloy Inconel 718. *Materials Science and Engineering A, 383*, 201–212. https://doi.org/10.1016/j.msea.2004.05.062.

Savrai, R. A., Makarov, A. V., Soboleva, N. N., et al. (2016). The behavior of gas powder laser clad NiCrBSi coatings under contact loading. *Journal of Materials Engineering and Performance, 25*(3), 1068–1075. https://doi.org/10.1007/s11665-016-1925-7.

Sims, C. T., Stoloff, N. S., & Hagel, C. (1987). *Superalloys II*. New York: Wiley.

Sui, S., Chen, J., Fan, E. X., Yang, H. O., Lin, X., & Huang, W. D. (2017a). The influence of laves phases on the high-cycle fatigue behavior of laser additive manufactured Inconel 718. *Materials Science and Engineering A, 695*, 6–13. https://doi.org/10.1016/j.msea.2017.03.098.

Sui, S., Chen, J., Ming, X. L., Zhang, S. P., Lin, X., & Huang, W. D. (2017b). The failure mechanism of 50% laser additive manufactured Inconel 718 and the deformation behaviour of laves phases during a tensile process. *International Journal of Advanced Manufacturing Technology, 91*, 2733–2740. https://doi.org/10.1007/s00170-016-9901-9.

Sui, S., Chen, J., Ma, L., Fan, W., Tan, H., Liu, F., & Lin, X. (2019). Microstructures and stress rupture properties of pulse laser repaired Inconel 718 superalloy after different heat treatments. *Journal of Alloys and Compounds, 770*, 125–135. https://doi.org/10.1016/j.jallcom.2018.08.063.

Wang, K. L., Zhang, Q. B., Sun, M. L., & Zhu, Y. M. (1977). Effect of laser surface cladding of ceria on the wear and corrosion of nickel-based alloys. *Surface and Coating Technology, 96*, 267–271.

Wang, K. L., Zhang, Q. B., Sun, M. L., Wei, X. G., & Zhu, Y. M. (2001). Rare earth elements modification of laser-clad nickel based alloy coatings. *Applied Surface Science, 174*(3), 191–200. https://doi.org/10.1016/S0169-4332(01)00017-4.

Wang, Z., Guan, K., Gao, M., Li, X., Chen, X., & Zeng, X. (2012). The microstructure and mechanical properties of deposited-IN718 by selective laser melting. *Journal of Alloys and Compounds, 513*, 518–523. https://doi.org/10.1016/j.jallcom.2011.10.107.

Wang, L., Song, S. Y., Hu, Y., et al. (2015a). Regulation research on microstructure of laser cladding under electric-magnetic synergistic effect. *Chinese Journal of Lasers, 42*, s103005.

Wang, L., Yao, J. H., Hu, Y., et al. (2015b). Suppression effect of a steady magnetic field on molten pool during laser remelting. *Applied Surface Science, 351*(11), 794–802. https://doi.org/10.1016/j.apsusc.2015.05.179.

Wang, L., Yao, J. H., Hu, Y., et al. (2017). Influence of electric-magnetic compound field on the WC particles distribution in laser melt injection. *Surface and Coating Technology, 315*, 32–43. https://doi.org/10.1016/j.surfcoat.2017.01.116.

Wolff, S. J., Gan, Z., Lin, S., Bennett, J. L., Yan, W., Hyatt, G., Ehmann, K. F., Wagner, G. J., Liu, W. K., & Cao, J. (2019). Experimentally validated predictions of thermal history and microhardness in laser-deposited Inconel 718 on carbon steel. *Additive Manufacturing, 27*, 540–551. https://doi.org/10.1016/j.addma.2019.03.019.

Wu, H., Zhang, D., Yang, B., Chen, C., Li, Y., Zhou, K., Jiang, L., & Liu, R. (2020). Microstructural evolution and defect formation in a powder metallurgy nickel-based superalloy processed by selective laser melting. *Journal of Materials Science and Technology, 36*, 7–17. https://doi.org/10.1016/j.jmst.2019.08.007.

Xiao, H., Li, S., Han, X., Mazumder, J., & Song, L. (2017). Laves phase control of Inconel 718 alloy using quasi-continuous-wave laser additive manufacturing. *Materials and Design, 122*, 330–339. https://doi.org/10.1016/j.matdes.2017.03.004.

Zhai, L., Wang, Q., Zhang, J., & Ban, C. (2019a). Effect of alternating current electric field on microstructure and properties of laser cladding Ni–Cr–B–Si coating. *Ceramics International, 45*(2019), 16873–16879. https://doi.org/10.1016/j.ceramint.2019.05.230.

Zhai, L. L., Ban, C. Y., & Zhang, J. W. (2019b). Investigation on laser cladding Ni-base coating assisted by electromagnetic field. *Optics and Laser Technology, 114*, 81–88. https://doi.org/10.1016/j.optlastec.2019.01.017.

Zhai, L. L., Ban, C. Y., & Zhang, J. W. (2019c). Microstructure, micro-hardness and corrosion resistance of Ni-Cr-B-Si coatings under electromagnetic field auxiliary laser cladding. *Surface and Coating Technology, 358*, 531–538. https://doi.org/10.1016/j.surfcoat.2018.11.034.

Zhang, S. H., Li, M. X., Cho, T. Y., Yoon, J. H., Lee, C. G., & He, Y. Z. (2008a). Laser clad Ni-base alloy added nano- and micron-size CeO_2 composites. *Optics and Laser Technology, 40*, 716–722. https://doi.org/10.1016/j.optlastec.2007.10.007.

Zhang, S. H., Li, M. X., Yoon, J. H., & Cho, T. Y. (2008b). Characterization on the coatings of Ni-base alloy with nano- and micron-size Sm_2O_3 addition prepared by laser deposition. *Materials Chemistry and Physics, 112*, 668–674. https://doi.org/10.1016/j.matchemphys.2008.06.024.

Zhang, Y. Z., Tu, Y., Xi, M. Z., et al. (2008c). Characterization on laser clad nickel based alloy coating on pure copper. *Surface and Coating Technology, 202*(24), 5924–5928. https://doi.org/10.1016/j.surfcoat.2008.06.163.

Zhang, D., Niu, W., Cao, X., & Liu, Z. (2015). Effect of standard heat treatment on the microstructure and mechanical properties of selective laser melting manufactured Inconel 718 superalloy. *Materials Science and Engineering A, 644*, 32–40. https://doi.org/10.1016/j.msea.2015.06.021.

Zhang, N., Liu, W. W., Deng, D. W., et al. (2018). Effect of electric-magnetic compound field on the pore distribution in laser cladding process. *Optics and Laser Technology, 108*, 247–254. https://doi.org/10.1016/j.optlastec.2018.06.037.

Zhao, J., Wang, G., Wang, X., Luo, S., Wang, L., & Rong, Y. (2020). Multicomponent multiphase modeling of dissimilar laser cladding process with high-speed steel on medium carbon steel. *International Journal of Heat and Mass Transfer, 148*, 118990. https://doi.org/10.1016/j.ijheatmasstransfer.2019.118990.